A Multi-Scale Model for Nickel-Based Oxygen Carrier in Chemical-Looping Combustion

by

Huabei You

A thesis
presented to the University of Waterloo
in fulfillment of the
thesis requirement for the degree of
Master of Applied Science
in
Chemical Engineering

Waterloo, Ontario, Canada, 2019

I hereby declare that I am the sole author of this thesis. This is a true copy of the thesis, including any required final revisions, as accepted by my examiners.

I understand that my thesis may be made electronically available to the public.

Abstract

The selection of oxygen carrier (OC) particles is crucial for the development of chemical-looping combustion (CLC) technology. Common OC particle models often involve first-order chemical reactions with respect to the concentration of fuel gas, which may not be able to account for the complex reaction mechanisms taking place on the contacting surface between gas and solid reactants.

In this work, we apply a multiscale modelling framework on NiO-based OC particle in order to explicitly consider and understand the effect of reaction kinetics. The proposed multiscale model consists of gas diffusion model and surface reaction. Continuum equations are used to describe the gas diffusion inside OC particles, whereas mean-field approximation and kinetic Monte Carlo methods are adopted to simulate the microscale events, such as molecule adsorption and elementary reaction, occurring on the contacting surface. These sub-models communicate through a boundary condition that defines the mass fluxes of both reactant and product gas species. Surface reaction mechanisms and the corresponding reaction rate constants considered in the present work are obtained from a systematic density functional theory (DFT) analysis.

The qualititive comparison with experimental data available in the literature suggests that the kMC-based multiscale model is able to provide better results than the MFA-based counterpart. A sensitivity analysis on the rate constants of key elementary reactions, length of intra-particle pore, and particle porosity was conducted to assess the effect of reaction kinetics and mass transport on the overall reaction process and validate the proposed multiscale model. The simulation results show reasonable tendencies and responses to changes in these modelling parameters, which indicates that the proposed multiscale modelling scheme on OC particle is suitable. To the author's knowledge, this is the first implementation of a multiscale model in CLC technology.

Acknowledgements

I would like to give my sincere gratitude to my supervisor, Professor Luis Ricardez Sandoval, who made this work possible. His professional advice and heart-warming encouragement have always been the most important things in all stages of this work.

Besides my advisor, I would like to thank the rest of my thesis committee: Prof. Croiset and Prof. Pritzker, for their insightful questions and constructive comments.

I thank my officemate Yue for sharing her valuable research results with me; my friend Donovan for helping me getting started with my research; and my fellow group members: Bohua, Grigoriy, Han, Honghao, Ilse, Jingde, Kavitha, Mahshad, Manuel, Marco, Mina, Oscar, Suhyoung, Yael for all the good memories we have created together.

I am profoundly grateful to parents for their unconditional love and support. My thanks extend to my grandparents who always care for me. Special thanks are due to Yi Huang who helped me when I was applying to study in University of Waterloo.

Finally, I want to give a big shout-out to KWCG Pokemon Go Community, especially the following trainers: kigesui, blazikeenn, Peetarded, Waynaro, hoohoolooloo, tpxtqx, lby3332010, zyr76392608, JonixxxEthan, hangrybox, sirpau1, SQL, Needaklu, Taurress, GotchaHundo, Trainer282828, DaTrippyWizard, ShadyGil, GravebornMuse, Surenix and everyone I have played with. We have driven across the town in the dawn of spring and chilled around a picnic table in the summer sunset; we have looped around campus when the leaves were falling and trekked along trails covered with glistening snow. I would like to thank all of you, for making the past two years a bless to me.

Table of Contents

List of Tables

List of Figures

List of Symbols

A_s Area of the simulated lattice surface 35

C_i Concentration of gas i in the pore 26

C_s Surface site density 32

$\mathcal{D}_{K,i}$ Knudsen diffusivity of gas i 26

$\mathcal{D}_{e,i}$ Effective diffusivity of gas i in the pore 26

$\mathcal{D}_{m,i}$ Molecular diffusivity of gas i 26

$\mathbf{J}_{i,enter}$ Mass flux of gas species i entering the gas phase from the surface 27

$\mathbf{J}_{i,leave}$ Mass flux of gas species i leaving the gas phase and absorbing onto the surface 27

$\mathbf{J}_i$ Mass flux of gas species i above the surface 26, 27, 32, 33

L Pore length 26

M_S Molecular weight of solvent S 27

M_i Molecular weight of gas i 27

N_A Avogadro constant 32

$\mathbf{N}_{avail,s}$ Number of available adsorption sites on the surface 27

N_j Number of lattice sites occupied by adsorbate j 34

N_n Number of empty lattice sites with n nearest neighbor(s) 34

N_p Number of particles involved in the reation 26

P Pressure 27

R Pore radius 26

Sh Sherwood number 27

S_p Surface area of a single OC particle 26

T Temperature 27

V Volume of the reacting space 26

$W_{a,i,n}$ Probability of gas species i adsorbs on an empty site that has n nearest neighbors 34

$W_{r,i}$ Probability of adsorbate j reacts with the exposed oxygen atom and form the product 34

d_{par} Particle diameter 27

ε Porosity of the OC particle 26

η_i Number of molecule i adsorb on or release from the surface 35

f Effect of lateral interaction 34

$k_{a,i}$ Adsorption rate constant of surface species i 27, 34

$k_{g,i}$ External mass transfer coefficient of gas species i 26

$k_{r,i}$ Reaction rate constant of surface species j 27, 34

n_s Number of surface species 31

ν_i Diffusion parameters of the diffusing species i. 27

r Radial direction of the pore 26

τ Current time of one KMC simulation 33, 35

θ_i Surface coverage fraction of species i 31

z Axial direction of the pore 26

Chapter 1

Introduction

Chemical-looping combustion (CLC) is one of the most promising greenhouse gas emission control technologies. The concept of chemical looping involves the use of a metal oxide as the oxygen carrier (OC) which continuously circulates between a fuel-reactor, where the OC provides oxygen to burn the fuel, and an air-reactor, where the OC is oxidized with air. Compared to the traditional fuel combustion process, CLC does not require extra separation units to obtain a pure CO_2 stream, thus minimizing the energy penalty associated with the CO_2 capture process.

In order to design, optimize, and eventually scale-up the CLC process, a variety of fuel- and air-reactors models have been developed. The three main parameters for the design of these reactors are: (1) the total load of bed material comprised of OC particles; (2) the circulation rate of bed material; and (3) the gas flow between the two reactors [1]. The first two parameters directly depend on the performance of the selected oxygen carrier. Consequently, the design of OC material is critical for the development of CLC technology.

The ideal OC should have the following properties: high reactivity, resistance against carbon deposition, high mechanical strength, and sufficient stability in successive cycle reactions. Aiming at developing OC materials with all the desired properties, numerous experiments on the reactivity of oxygen carrier particles have been conducted over the last decades [2, 3, 4, 5, 6, 7]. These studies have shown that the reactivity of the carriers varies considerably depending on the material, particle size, fuel gas, and operating temperature. Thus, in order to develop a suitable oxygen carrier material, it is necessary to test many materials with varying metal oxide/support combinations and production conditions, which is labour-intensive, impractical and overly expensive. Thus, having access to an OC model that can evaluate the effect of the different reaction kinetics on the overall performance of

the OC particle will greatly help in the design of OC particles and enhance the technical viability of CLC technology for CO_2 capture and clean power generation.

The most common OC models available in the literature are the shrinking unreacted core model[8], the changing grain size model [9], and the nucleation and nuclei growth model [10]. These models have been used to simulate the temperature and conversion profiles inside some commonly used oxygen carriers during the CLC process. They have assumed that the concentration of gas reactant only varies in one direction that is normal to the particle surface. Similarly, they also consider that the chemical reactions taking place in the particle are first order reactions with respect to the concentration of gas species. In a real setting, concentration profiles in both axial and radial directions exist when the gas (*i.e.*, the fuel) diffuses through the particle's pore. Moreover, reactions are actually taking place on the solid surface, and the mechanism is generally more complex than first order reactions. Therefore, these models may not be able to completely describe the effect of radial concentration gradients across the pore and the complexity of reaction kinetics which, as suggested by experimental results, plays an important role and should be taken into account when developing oxygen carrier particle models [11, 12, 13, 14].

The difficulty in modelling the impact of reaction kinetics lies in the discrepancies between the evolution of the chemical reactions on the particle pore surface and the continuum mechanics that describes the transport of molecules in the gas phase. Specifically, the gas diffusion in the pore occurs at a micrometer length scale whereas surface events usually take place in nanoscale (molecular) dimensions. In addition, the corresponding time scale for the chemical reactions is also orders of magnitude smaller than that for gas diffusion. As a result, simulating gas diffusion and surface reaction simultaneously throughout the whole time and spacial domains is computationally intensive, if not prohibitive. A compromise approach is that one does not solve the nanoscale (microscale) model over the entire computational domain; instead, multiple microscale models are solved repeatly during the simulation. Since the macroscale model is typically described by continuum equations solved by numerical methods involving domain discretization, the effect of spatial variants of macroscopic properties (*e.g.* concentration) on microscale events is taken into account by placing multiple microscale models at different discretized points and solving them locally. The coarse-grained information of the microscale model is then interpreted throughout the spatial domain and lifted to the higher scale model, providing data needed to solve the macroscale dynamics.

A model comprising sub-models that conserve and pass information at multiple scales is referred to as a multiscale model. This modelling approach is capable of predicting the effect of reaction kinetics taking place inside the particle on the overall performance of OC particles, and make it possible to compare or even design different materials and estimate

their viability as oxygen carriers for industrial applications. To the author's knowledge, a multiscale model for OC particles in CLC process has not been proposed in the literature.

Research Objectives

In order to apply the multiscale modelling framework for OC particles in the CLC process, continuum equations are used to describe gas transport inside the OC particle (macroscale model), whereas mean-field approximation (MFA) and kinetic Monte Carlo (kMC) methods are used to model the surface reaction kinetics (microscale model), respectively. Nickel oxide and syngas (CO and H_2) are selected as the solid reactant in the OC particle and the fuel gas, respectively. This system has been commonly used in laboratory and pilot-scale demonstration plants. Surface reaction mechanism considered in the microscale model and kinetic parameters such as reaction rate constants have been estimated from density functional theory (DFT) analysis. The main objectives in this work are to:

- Develop a macroscale model describing gas transport inside the OC particle.
- Establish the fundamental surface reaction steps and calculate the corresponding elementary reaction rate constants using density functional theory (DFT).
- Develop two microscale models describing the gas-solid reactions on solid reactant surface using mean-field approximation method and kinetic Monte Carlo method, respectively.
- Develop a multiscale model that can explicitly account for the effect of surface reaction kinetics on the overall OC particle performance.

As mentioned above, This work presents the first multiscale model for OC particles. The modelling framework can be adopted to model other systems, thus providing a new approach to compare the effect of fuel gas, OC material, and operating conditions. It also enables the possibility of theoretically predicting the performance of a potential OC material, which can provide insights for the design of new materials.

Thesis Outline

This thesis is organized as follows: the next chapter provides a detailed review of the common CO_2 capture technologies and recent developments of oxygen carriers, as well

as the theories applied in this research, *e.g.* MFA method, kMC method, and multiscale modelling approaches. Chapter 3 presents a multiscale model that consists of macroscale gas transport and microscale surface reaction. The macroscale model is developed based on continuum equations to describe the intra-particle gas diffusion. Then, the microscale model describing reactions taking place on the contacting surface between gas and solid reactants is developed based on the MFA and kMC methods, respectively. These two surface-based models are then coupled with the gas transport model to simulate the dynamic performance of an OC particle. Furthermore, a comparison between MFA-based and kMC-based multiscale model is presented, followed by the comparison between simulation results and experimental data reported in the literature, and lastly by a sensitivity analysis on key modelling parameters. Concluding remarks and future research directions are given in Chapter 4.

Chapter 2

Literature Review

This chapter presents an overview of previous work on related literature and studies conducted by academics and industrial practitioners that provide the necessary background to develop this research. This chapter is organized as follows: the first section provides an up-to-date report of CO_2 emissions; the second section gives an overview of the advantages and limitations of the common CO_2 capture technologies including one of the most promising CO_2 capture technology - chemical-looping combustion (CLC); the third section explains the important role of the oxygen carrier (OC) in this technology and also lists the recent laboratory and modelling work related to OC development; the fourth section provides details of the modelling scheme (multiscale model) proposed in this research and the commonly applied techniques.

2.1 CO_2 emissions - an urgent environmental problem

The carbon dioxide (CO_2) concentration in the atmosphere has increased significantly over the past few decades due to the increasing use of fossil fuels as the main source of energy. According to the document entitled State of the Climate [15], the global average atmospheric carbon dioxide concentration in 2017 (405.0 parts per million (ppm)) was the highest in at least the past 800,000 years. That same year was also the second or third warmest year (depending on the dataset used) since records began in the mid 1800s, with the annual global surface temperatures 0.38 °C-0.48 °C above the 1981-2010 average. At the same time, global mean sea levels have risen for the sixth consecutive year, reaching the highest annual average in the satellite altimetry era (since 1993). Climate change can

only be mitigated and global temperature be stabilized when the total amount of CO_2 emitted is limited and annual emissions eventually approach zero [16, 17].

The Intergovernmental Panel on Climate Change (IPCC) Fifth Assessment Report (AR5) showed that in 2010, the energy generation sector was the largest contributor (around 35%) to global greenhouse gas (GHG) emissions, followed by industry which contributed 30% of global GHG emissions. These two sectors have been using fossil fuel as their main energy source and generating CO_2, the main GHG, during the combustion process. Therefore, CO_2 capture and storage is considered as a critical technology to significantly curb the amount of CO_2 in atmosphere.

2.2 CO_2 capture technologies

Three main CO_2 capture technologies are currently available: post-combustion, pre-combustion, and oxyfuel combustion. In post-combustion capture, CO_2 is separated and then captured from flue gas after the fossil fuel has been burned. The most common method involves using a solvent to selectively absorb CO_2 from the flue gas, followed by CO_2 desorption process in a stripping column to regenerate the solvent. High temperature is needed in order to separate the absorbed CO_2 from the solvents (typically amines), which requires a large amount of extra energy input. The energy penalty associated with the solvent regeneration process is the main challenge in post-combustion technology that must be overcome in order to make this technology more pratical and appealing for large scale deployment.

In pre-combustion capture, carbon is removed from the fossil fuel before combustion, resulting in a carbon-free flue gas. The carbon removal is usually achieved by gasifying solid fuel to form synthesis gas which then undergoes the water-gas shift reaction to convert CO and H_2O to CO_2 and H_2. After separating and capturing CO_2, the pure H_2 stream is sent to the combustion sector. Compared to post-combustion technology, which removes CO_2 from flue gas that has a low CO_2 concentration and pressure, the gasification and water-gas shift process produces a high pressure, CO_2-rich gas mixture, which does not require extra energy to capture CO_2. However, the capital costs of the equipment for this technology are often expensive, which hinders its application. Moreover, the solid fuel gasification process is not energy-free.

Oxyfuel combustion is a process of burning fossil fuels with an oxygen-enriched gas mixture instead of air. This results in a flue gas that mainly comprises CO_2 and H_2O, which can be easily separated by a condensation process that does not require external energy input. Chemical-looping combustion (CLC) is one of the most promising oxyfuel

combustion technologies [18]. The concept of CLC was firstly introduced by Ishida *et al.* in 1987 [19]. In CLC systems, oxygen is introduced to the system via oxidation-reduction cycling of an oxygen carrier (OC). The oxygen carrier is usually a solid, metal-based particle. For a typical CLC process, combustion is split into separate reduction and oxidation reactions in multiple reactors. The metal oxide particles supply the oxygen needed for combustion and are reduced by the fuel in the fuel reactor, these particles are then transported back in the air reactor to react with air to continue to the next cycle. The gas existing the air reactor contains N_2 and unreacted O_2, whereas the flue gas of the fuel reactor contains CO_2 and H_2O (See Fig 2.1).

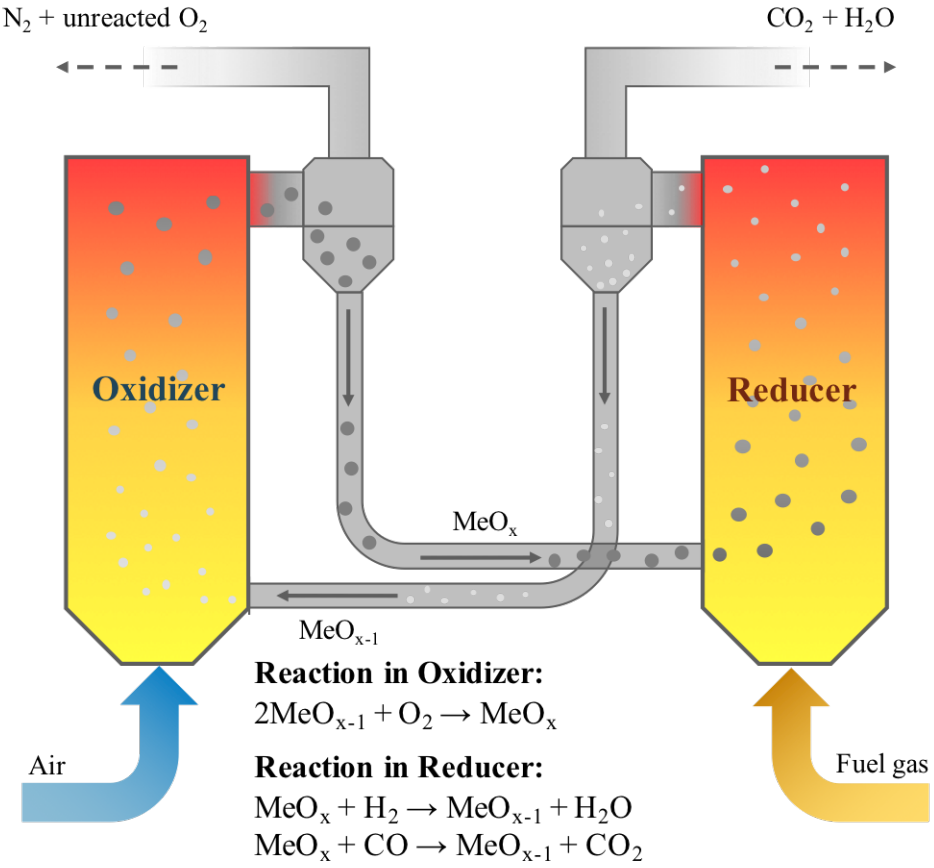

Figure 2.1: CLC scheme

One of the key elements for the industrialization of CLC technology is the high durability and consistent performance of OC particles in long-time successive operating cycles

[20]. The OC must fulfill a range of requirements, including: high reactivity in both air and fuel reactors; sufficient stability at high temperature, strong resistance against carbon decomposition, and high mechanical strength [21]. Major efforts are hence dedicated to identifying suitable carriers and increasing the activity and robustness of candidate materials. Discussion about the experimental and the modelling studies focused on improving the performance of OC particles is presented in the next section.

2.3 Experimental Studies on OC

A large number experimental studies have been conducted on oxygen carrier particles. Most of the OC materials being investigated are made of an active metal oxide (NiO, CuO, Fe_2O_3, MgO, MnO_2, *etc*) and a supporting inert material (Al_2O_3, $MgAl_2O_4$, $NiAl_2O_4$, TiO_2, SiO, stabilized ZrO_2, bentonite, sepiolite, *etc*). Researchers have also studied the potential of using natural minerals such as iron ore, ilmenite ore, manganese ore to replace synthetic materials more recently [22, 23, 24, 25]. Based on results and analysis reported in the literature, it is widely acknowledged that OC particles based on Ni exhibit superior reactivity and stability. Hence, Ni-based materials have became one of the most widely investigated materials [26, 27, 28, 29, 30, 13]. In order to have a better comparison with the experimental data, NiO is chosen as the active oxide for the multiscale model proposed in this work. Details about relevant experimental work are discussed below.

Ni-based oxygen carriers

Significant efforts have been made to investigate the potential of Ni-based oxygen carriers. Ishida *et al.* [31] used thermogravimetric analysis (TGA) to investigate the reaction rate of NiO/YSZ (yttria-stabilized zirconia) particles with a stream of H_2. They further studied the effects of the solid composition, feed gas composition and reaction temperature on carbon deposition on the basis of NiO/YSZ particle in a thermogravimetric reactor (TGR) [32]. They concluded that the reaction temperature, particle size, gas composition, and solid composition all strongly affect the overall reaction rate, especially the effect of solid composition on reduction rate.

Villa *et al.* [33] investigated the performance of OC particles made of Ni-based mixed oxide materials (Ni-Al-O system and Ni-Mg-Al-O system) under redox cycle conditions. Experiments were conducted using repeated temperature-programmed reduction (TPR) and temperature-programmed oxidation (TPO) cycles with CH_4 and H_2 as reducing gas

and O_2 as oxidizing gas. The results showed that the addition of Mg improved the redox stability and resistance to coke formation. The Ni-Mg-Al-O system has also demonstrated a high tendency to form CO and H_2 instead of CO_2 and H_2O when CH_4 was used as fuel gas, which makes it a candidate for syngas production. Mattisson *et al.* [28] studied the reactivity of four different Ni-based OC particles with CH_4 fuel gas. The experiments were conducted in a laboratory-size fluidized bed reactor. All investigated particles showed high rates of reduction with no sintering tendencies during reaction and limited or no particle breakage. Gayán *et al.* [34] measured the reactivity of NiO/Al_2O_3 OC particles prepared by different methods in a thermogravimetric analyzer. The data suggested that Ni-based OC prepared on α-Al_2O_3 has higher reduction reactivity than the OC prepared on γ-Al_2O_3. Also, particles prepared on α-Al_2O_3 exhibited very high reactivity during both reduction and oxidation reactions.Sedor *et al.* [35] investigated OC with various Ni loadings on an α-Al_2O_3 support. TPR and TPO were employed to evaluate the reactivity and stability of different OC samples in repeated redox cycles. The result showed that particle samples with higher nickel loading (up to 20%) provided more oxygen for reduction in the form of NiO. Also, consistent Ni dispersion inside particle was observed during successive redox cycles and no agglomeration was found. Shen *et al.* [30] reported the deterioration of reactivity of NiO/α-Al_2O_3 OC during 100 hours of operation in a 10 kW_{th} continuous reactor of interconnected fluidized beds using coal as fuel. Further analysis showed that sintering occurred when the temperature in the fuel reactor exceeded 960 °C. However, this problem can be mitigated by supplying steam to the fuel reactor. Dueso *et al.* [36] used TGA and a batch fluidized bed reactor to study the reactivity of NiO/α-Al_2O_3 OC during successive redox cycles with CH_4 as fuel gas. They observed that the reactivity of OC decreases with increasing solid conversion due to the formation of $NiAl_2O_4$ during oxidation. However, high conversion of fuel gas was still achieved in the experiment. They also investigated the reactivity of two Ni-based oxygen carriers (NiO/α-Al_2O_3 and NiO/γ-Al_2O_3) at different fuel concentrations (5 - 20 vol.% CH_4, 5 - 50 vol.% H_2 and CO) and temperatures. Differences in reaction kinetics were observed, which are likely caused by the different structure of alumina support.

2.4 Common OC Models

Although intensive efforts have been invested in experiments and have also yielded significant results, many materials must be examined. In addition, different operating conditions such as temperature and pressure can also affect the performance of OC materials. Therefore, it is not efficient to completely rely on experiments to find the ideal OC for varies

operating conditions for which CLC is suitable. On the other hand, having access to a reliable theoretical model that can accurately describe the behavior of OC particles in CLC reactors will further advance our understanding of the determining factors and even provide useful infomation to improve the design of current OC. The reations involving OC particles in air and fuel reators can be considered as non-catalytic gas-solid reactions that can be expressed as follows:

$$aA(g) + B(s) \rightarrow bP(s) + cCO_2(g) + dH_2O(g), \tag{2.1}$$

In reality, this overall reaction equation typically involves several intermediate steps: (1) fuel gas diffusion from the bulk gas phase to the surface of the solid particle, (2) diffusion of the fuel gas through the pores of the particle; (3) adsorption of reactants on the pore surface and (4) chemical reactions between the gas and the solid. Different models for gas-solid reactions have been developed to predict the performance of different OC particles. The most frequently used models that describe the gas-solid reaction takes place inside the OC particle are the changing grain size model (CGSM), the shrinking core model (SCM), and the nucleation and nuclei growth model (NNGM) (See Fig 2.2).

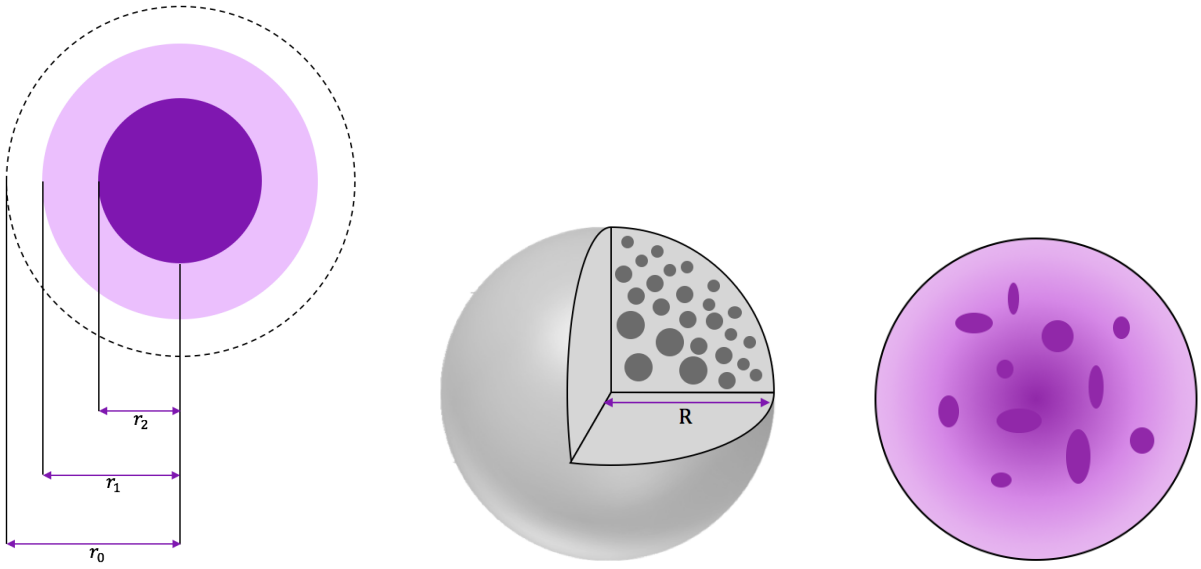

(a) SCM (b) CGSM (c) NNGM

Figure 2.2: Common OC particle models.

Shrinking Core Model (SCM)

The shrinking core model (SCM) is characterized by a clearly defined shrinking reaction interface in a particle between the porous product outer layer and the non-porous unreacted core. Initially, the reaction happens in the external surface of the particle. As the reaction proceeds, an interface between the unreacted core and reacted solid, on which all chemical reactions take place, is formed and keeps moving inward; hence, the unreacted core keeps shrinking. Before reaching the surface of the unreacted core, the fuel gas diffuses through the gas film between the bulk gas phase and the OC particle surface and the solid product film. The mass transfer equation considering the diffusion through the product layer and reactions on the core surface is as follows:

$$\frac{d}{dr}\left(-D_{e,A}r^2\frac{dC_A}{dr}\right)=0 \tag{2.2}$$

with the following boundary conditions:

$$C_A(r)\Big|_{r=r_0}=C_{A0} \tag{2.3}$$

$$C_A(r)\Big|_{r=r_2(t)}=0 \tag{2.4}$$

where C_A is concentration of gas species A, r is radius direction of the particle, $D_{e,A}$ is effective diffusion coefficient of gas species A, C_{A0} is concentration of gas species A in the bulk, r_0 is initial radius of the particle, and r_2 is radius of the unreacted core.

Solution of the transport equation (2.2) leads to the following expression for the rate of advance of the radius of the unreacted core r_2 [37]:

$$\frac{dr_2}{dt}=-\frac{aC_{A0}/\rho_B}{\frac{r_2^2}{r_0^2k_g}+\frac{(r_0-r_2)r_2}{r_0D_e}+\frac{1}{k_s}} \tag{2.5}$$

where a is the stoichiometric coefficent of fuel gas A, ρ_B is molar density of solid reactant B, k_g is the mass transfer coefficent for gas species A between the bulk gas and outer surface of the particle, k_s is reaction rate constant at the surface of the unreacted core.

The solid conversion X can be obtained as follows:

$$1-X=\left(\frac{r_2}{r_0}\right)^3 \tag{2.6}$$

The three terms in the denominator in Eq.2.5 represent the resistances due to gas-film diffusion, product layer diffusion and the chemical reaction, respectively. Ishida *et al.* [31] adopted the SCM to interpret data from experiments. It was found that the rate of reduction is controlled mostly by the chemical reaction, whereas the rate of oxidation is depend on both chemical reaction and the product layer diffusion. Ryu *et al.* [8] also employed SCM to describe the reaction of air and CH_4 with Ni/bentonite particle. The reaction rate constant in that model was calculated from experimental data and fitted to the Arrhenius equation. The simulation results fitted the experimental data with reasonable agreement.

Changing Grain Size Model (CGSM)

Initially proposed by Georgakis *et al.* [38], the changing grain size model assumes that the particle consists of a number of non-porous grains of uniform radius r_0. Each grain follows the scheme depicted by SCM. The fuel gas must overcome the resistances in gas-film diffusion, diffusion through the interstices between the grains, diffusion through the product layer of the grain, and chemical reaction on the surface of the unreacted core. The unsteady-state mass transfer equation considering the reaction within the particle can be formulated as follows:

$$\frac{\partial C_A}{\partial t} = \frac{1}{R^2}\frac{\partial}{\partial R}(D_{e,A}R^2\frac{\partial C_A}{\partial R}) - (-r_A) \tag{2.7}$$

with the following initial and boundary conditions:

$$C_A(R,t)\Big|_{t=0} = C_{A,b} \tag{2.8}$$

$$\frac{dC_A}{dR}\Big|_{R=0} = 0 \tag{2.9}$$

$$-D_{e,A}\frac{dC_A}{dR}\Big|_{R=R_0} = k_g(C_{A,s} - C_{A,b}) \tag{2.10}$$

where R is the radial coordinate of the particle, $C_{A,b}$ is gas concentration in the bulk phase, k_g is external mass transfer coefficient, $C_{A,s}$ is gas concentration at the external surface of the particle.

The reaction rate per unit of particle volume is modeled such that is directly proportional to the chemical reaction rate constant, k:

$$\frac{1}{a}(-r_A) = (-r_R) = kS_{0,R}(\frac{r_2}{r_0})^2 C_A \tag{2.11}$$

where is r_0 the initial radius of the grain, r_2 is radius of the unreacted core, and $S_{0,R}$ is the initial specific surface area of the reactant.

García-Labiano *et al.* [9] adopted this model to estimate the relative relevance of different steps in the reaction of OC particles in CLC applications. The resistance to heat and mass transfer in the gas film and inside the particle together with the chemical reaction on the particle surface were considered for the oxidation and the reduction reactions with different fuel gases (CH_4, H_2 and CO) and materials (Ni, Cu, Fe, Mn, and Co). Chemical reaction rate constant k was assumed to be an Arrhenius type function of temperature. The effect of k on the particle temperature was analyzed by variations in the preexponential factor (k_0) and in the activation energy (E_a). They reported that both preexponential factor and activation energy did not significantly affect the conversion and temperature profiles within the particle.

Nucleation and nuclei growth model (NNGM)

According to the nucleation and nuclei growth model (NNGM), the gas-solid reactions within the OC particle proceed with the generation of metallic nuclei, which subsequently grow and finally overlap. Hossain *et al.* [10] adapted the Avrami-Erofeev model to describe the change rate of the degree of conversion X as:

$$\frac{dX}{dt} = k(T)f(X) \tag{2.12}$$

where k is the rate constant given by the Arrhenius equation as a function of temperature T, and $f(X)$ is a function of the degree of conversion given as:

$$f(X) = \nu(1-X)[-ln(1-X)]^{(\nu-1)/\nu} \tag{2.13}$$

where ν is the Avrami exponent indicative of the reaction mechanism and crystal growth dimension. For example, $\nu = 1$ for the random nucleation model, and $\nu = 2$ or 3 for 2-dimensional or 3-dimensional nuclei growth, respectively.

The kinetic parameters used in this model were obtained using the hydrogen and oxygen consumption data from the temperature programmed reduction or oxidation (TPR/TPO) profile analysis. The conversion in this model is defined as follows:

$$X = \frac{\Delta n_t}{\Delta n_{total}} \tag{2.14}$$

where Δn_t represents the moles of H_2 or moles of O_2 consumed at time t and Δn_{total} represents the total moles of H_2 or moles of O_2 consumed for the complete reaction of the OC particle.

Sedor *et al.* [35] modeled the reduction kinetics of NiO/Al_2O_3 oxygen carrier using NNGM and SCM separately. The NNGM with $\nu = 1$ was found to give a better description of the experimental data. Hossain *et al.* [10] developed NNGM and SCM to describe reduction and oxidation kinetics of $Co - Ni/Al_2O_3$ oxygen carrier. Model parameters such as reaction rate constants were estimated using a least square fitting to the TPR/TPO data. Their results also suggested that NNGM has higher accuracy than SCM.

Based on the above, it is clear that all three common OC models mentioned need the data from experimental works (TGA, TPR, or TPO) to provide the reaction rate constants for all chemical reactions. These reaction rate constants are estimated such that the simulation results fit the experimental data. These models are then used to predict the performance of OC under other conditions. Therefore, the prediction is only valid when the changes in reacting conditions do not affect reaction rate constants, which is usually not true when variations exist in the operating temperature or when using different OC materials. In other words, new experiments must be conducted to calculate a new set of kinetic parameters for the new condition, which is very labor-intensive and expensive.

2.5 Multiscale Modeling Scheme

While it is difficult to bridge the gap between fundamental chemical reactions and realistic modelling through experiments, a new method driven by the modern computational power has emerged over the past few decades - first-principles calculation, also known as density-functional theory (DFT) [39, 40]. DFT is a method that approximates solution to the Shrödinger equation of a many-body system. It is the state-of-the-art theory to investigate the structural and electronic properties of molecules and materials. DFT has been successfully employed to predict the reaction path and kinetics of many systems including (but not limited to) CO oxidation on transition metal surfaces [41, 42, 43], ammonia synthesis over a nanoparticle ruthenium catalyst [44], water-gas-shift reaction on metal nanoparticles and surfaces [45] and methane cracking reaction pathways on Ni surface [46]. Despite being a powerful tool, DFT can not be directly applied in modelling reactions taking place in chemical reacting systems due to the time and length discrepancies between the evolution of the elementary chemical reactions and the continuous transport of the gas or fluid inside the system. At least three scales are involved in a typical gas-solid reaction: (i) the atomistic scale where the individual molecules interact with adsorbate or

other molecules, (ii) microscale (or surface scale) where elementary reaction events take place and (iii) macroscale (or particle scale) where the gradients in concentration of gas flow exist. As shown in Fig 2.3, these three scales form a hierarchical structure and also have their unique characteristic length and time scales. For example, size of a molecule is on the scale of Angstroms and it vibrates in the order of picoseconds, whereas the radius of a particle is generally several micrometers or even millimeters and the most commonly used time unit when describing gas transport is in the order of seconds. Consequently, it is currently prohibitive to scale up the DFT simulation by simple integration. The more appropriate application of DFT in the field of multiscale modelling is to provide the information required to calculate the reaction rate constant of each elementary reaction using transition state theory (TST) and narrow the discrepancy using a statistical technique that can average the collective behavior of all elementary reactions over length and time scales that are much larger than the characteristic length and time scales of the atomistic kinetics. The main techniques that can be used to bridge this gap are: (1) the molecular dynamics (MD) [47], (2) the mean-field approximation (MFA) [48], and (3) the kinetic Monte Carlo (kMC) methods [49]. MD simulates the moving trajectories of all atoms involved in the system by numerically solving Newton's equations of motion for each atom. The time scale of a typical MD simulation spans from nanoseconds to microseconds at a computational cost up to several CPU days [50]. On the other hand, MFA and kMC methods cannot provide information about the motion of all atoms in the system; instead, they give coarse-grained estimations about how system evolves in a time period ranging from microseconds to seconds. The present model employs TST, MFA and kMC methods to develop the microscale model. Detailed description of these methods are presented next.

Transition State Theory

Before introducing TST, it is necessary to explain two concepts, namely Born-Oppenheimer (BO) approximation [51] and a potential energy surface (PES) [52]. The BO approximation assumes that the electron interactions take place on much faster time scale than the motion of the atomic nuclei; thus, the motion of nuclei and electrons can be separated. Based on the BO approximation, the electrons in the system adapt adiabatically to every configuration of nuclei positions $\mathbf{r}$, and, reciprocally, for each nuclei configuration $\mathbf{r}$, the system has a different energy $E\{\mathbf{r}\}$, which is treated as a point on the PES landscape. In other words, PES describes the energy of a system, especially a collection of atoms, as a function of the positions of nuclei in the system. Therefore, for a molecule with N atoms, its PES has $3N-6$ coordinates (each atom has three coordinates x, y, and z, minus three

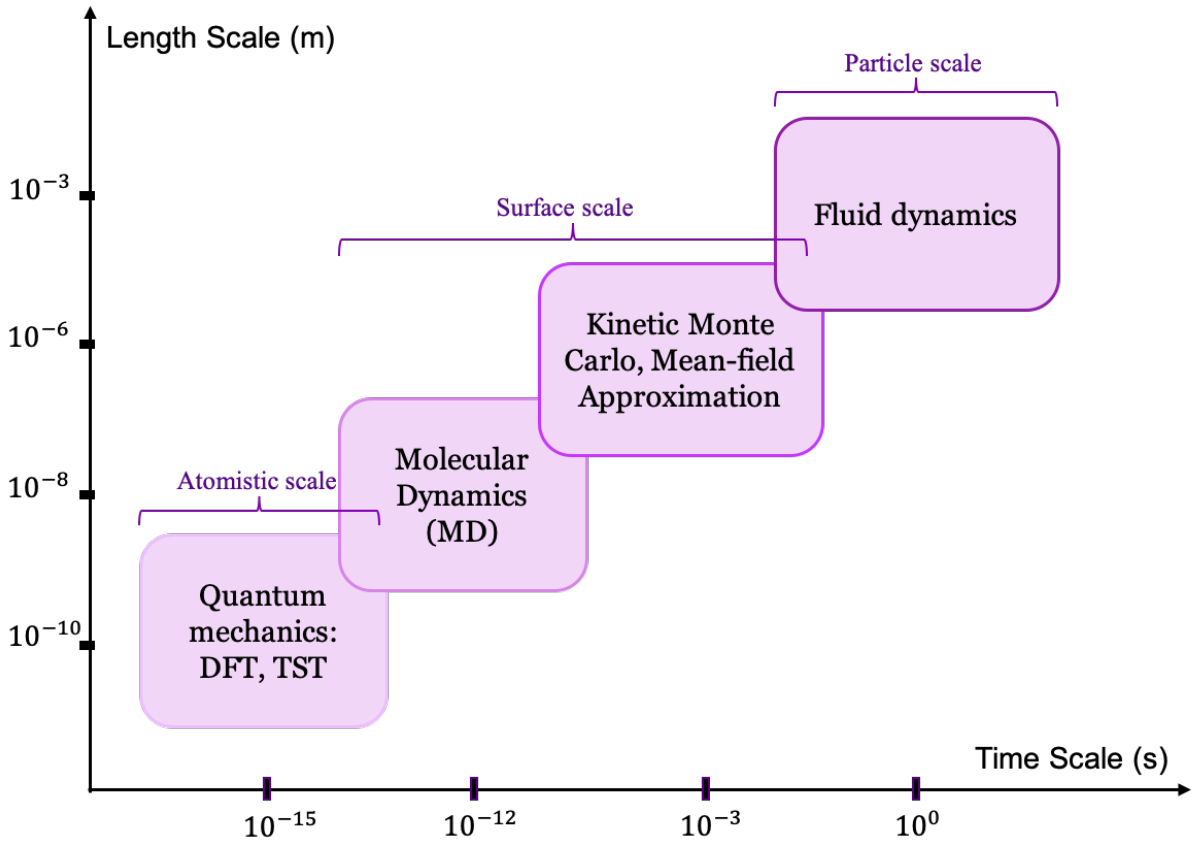

Figure 2.3: Hierarchical structure in multiscale modelling

molecule translation and three molecule rotation coordinates). The evolution of the atomic configuration can be described as the system evolves on the PES. The forces acting on a given configuration are then the local gradient of the PES, and the system maintains a (temporary) stable configuration when it dwells in a (local) minimum of this surface. The electronic level dynamics such as picosecond-scale vibrations, on the other hand, cause the system to wander around the local minima, but they may not be enough for the system to surmount the energy barrier between two minima. Because electrons move orders of magnitude faster than nuclei, the system spends most of the time in one of the basins on the PES before it accumulates enough energy to move to another basin or state. Similarly, one can assume that such a hypersurface must also exist for a reacting system, where the reactants and the products are two stable states of the system, which correspond to two local minima on the PES.

Another fundamental assumption in transition state theory is that for a general reaction:

$$A + B \longrightarrow P \tag{2.15}$$

the reactants firstly form an activated complex, which then transforms into the product. Therefore, the reaction equation can be re-written as:

$$A + B \rightleftharpoons (AB)^{\ddagger} \longrightarrow P \tag{2.16}$$

Combining the assumption of the existence of PES and the activated complex $(AB)^{\ddagger}$, the chemical reaction can be depicted as the system energy from the local minimum it originally dwells in (the reactant state) to the transition state where it is higher (the activated complex state), and finally drops into another local minimum (the product state). As illustrated in Figure 2.4, the highest point in this reaction path is called the saddle point, which represents the energy of the activated complex $(AB)^{\ddagger}$. The rate of reaction can be expressed as the product of the concentration of $(AB)^{\ddagger}$ ($[\frac{mol}{m^3}]$) and the frequency of $(AB)^{\ddagger}$ crossing the saddle point ($[\frac{1}{s}]$):

$$r = [AB]^{\ddagger}\nu \tag{2.17}$$

Assuming the formation of $(AB)^{\ddagger}$ is always at equilibrium, the $(AB)^{\ddagger}$ concentration can be expressed as follows:

$$[AB]^{\ddagger} = K^{\ddagger}[A][B] \tag{2.18}$$

where $K^{\ddagger}$ is the equilibrium constant. Therefore, the reaction rate becomes:

$$r = \nu K^{\ddagger}[A][B] \tag{2.19}$$

Compare Equation 2.19 to the general rate law:

$$r = k[A][B] \tag{2.20}$$

The reaction rate constant k can then be calculated as:

$$k = \nu K^{\ddagger} \tag{2.21}$$

The frequency of $(AB)^{\ddagger}$ crossing the saddle point can also be considered as the vibrational frequency for the vibration of the bond being formed or broken in the activated complex in order to form the products. The energy of the bond vibration is as follows:

$$E_{vi} = h\nu = k_B T \tag{2.22}$$

which gives the expression for ν as:

$$\nu = \frac{k_B T}{h} \tag{2.23}$$

where k_B is the Boltzmann constant, T is the temperature and h is the Plank constant.

The transition state equilibrium constant $K^{\ddagger}$ can be described as a statistical approach using partition functions of the reactant, the transition state and the product, *i.e.*, :

$$K^{\ddagger} = \frac{Q^{\ddagger}_{AB}}{Q_A Q_B} e^{-\Delta G^{\ddagger}/RT} \tag{2.24}$$

where $\Delta G^{\ddagger}$ is the standard Gibbs energy of activation, and Q_i is the partition function of species i per unit volume and its formula is derived using statistical mechanics.

Combining Eq.2.23 and Eq.2.24, the reaction rate constant can be expressed as follows:

$$k = \frac{k_B T}{h} \frac{Q^{\ddagger}_{AB}}{Q_A Q_B} e^{-\Delta G^{\ddagger}/RT} \tag{2.25}$$

Therefore, all that is required to obtain the reaction rate constant k at a certain temperature T are the values of $\Delta G^{\ddagger}$ and three partition functions. The values of parameters needed to calculate $\Delta G^{\ddagger}$ and Q_i can be obtained from first-principles calculation. More details can be found in references [53], [54], [55] and are beyoud the scope of this document.

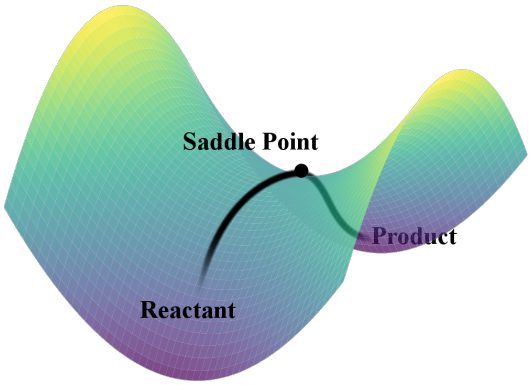

Figure 2.4: Potential Energy Surface

Mean-field Approximation

The mean-field approximation assumes a uniform distribution of adsorbate on a solid reacting surface. It links elementary surface reactions to particle level quantities by calculating the changes in surface coverage θ of each adsorbed species. The surface coverage of species A, θ_A, is defined as the fraction of the number of sites occupied by species A to the total number of possible adsorption sites on a surface of area S_0. The equation describing the rate of change of θ_A can be generally written as follows:

$$\frac{d\theta_A}{dt} = k_a C_{A,g} \theta_{empty} f(\theta_A) - k_d \theta_A g(\theta_A) - k_r \theta_A h(\theta_A) \tag{2.26}$$

where $C_{A,g}$ is the concentration of A in gas phase above the surface; k_a, k_d, and k_r are the respective rate constants for adsorption, desorption and reaction on the solid surface; the functions f, g, and h account for the effect of lateral interactions (*i.e.*, neighboring effects) between adsorbed molecules and are typically set to 1 under the assumption that the surface consists of identical non-interactng adsorption sites. The macroscale diffusion flux $\mathbf{J}_A$ for gas species A is determined by the concentration of A in the gas phase and the surface coverage at time t, *i.e.*,

$$\mathbf{J}_A = F\{C_{A,g}(t), \theta_A(t)\} \tag{2.27}$$

The mean-field model is capable of employing DFT-based rate constants to give a coarse-grain description of the surface evolution as well as reaction rates. This method is relatively efficient and easy to implement; however, the main drawback of MFA is that it ignores the effect of uneven adsorbate distributions and cannot reproduce the changes of reaction rate constants caused by lateral interactions. The kinetic Monte Carlo method, on the other hand, is able to retain such detailed information.

Kinetic Monte Carlo

As mentioned above, a small surface where gas-solid reactions take place can be viewed as a system of atoms and the configuration of this system is determined by the positions of all atoms on the surface. Changes in atom postions cause the system to move from one minima (basin) to the other (basin), but changes at the electronic level do not impact the total energy of the system. Thus, the system remains in a basin of the PES for a comparatively long period of time so that it is reasonable to assume that the system is not affected by its prior history when it moves to another state (basin). Also, for each possible state-to-state movement, a characteristic constant W_{ij}, in the units of sec^{-1} describes the

probability of the system moving from state i to state j. This constant is independent of the state prior to state i and is only affected by the shape of basin i, the saddle point between basin i and j, as well as basin j on the PES [56]. This behavior is also known as the Markov walk that can be described by a Markovian master equation [57]:

$$\frac{dP(i,t)}{dt} = -\sum_{j} P(i,t)W(i \to j,t) + \sum_{j} P(j,t)W(j \to i,t) \tag{2.28}$$

where $P(i/j,t)$ is the probability to find the system in state i/j at time t, $W(i \to j)$ is the transition rate from state i to state j at time t and vice versa.

According to the chemical master equation, if all energy basins on a PES and their corresponding transition probabilities are known, one can solve the master equation analytically and find the probability of the system in state a at time t. For a simple molecule such as H_2O, its PES is a three-dimensional surface. Therefore, given results from enough computer simulations, one can depict the shape of PES and find the analytical solution for the master equation. However, for a gas-solid reaction system that typically involves hundreds of atoms, the complexity of PES escalates rapidly and deriving an analytical solution is no longer possible. In this case, one can resort to solve the chemical master equation numerically. One of the popular methods to approximately solve the master equation is kinetic Monte Carlo (kMC) simulations.

The core of any kMC simulation is a stochastic algorithm that propagates the system from state to state. The underlying principle in this algorithm is the random selection of an event based on the transition rates of all possible events at a particular time, execution of the selected event (correctly change the system configuration, *i.e.*, state of the system), updating the event list and the transition rates and finally advancing the time clock. This procedure solves the master equation in the sense that the probability of the system in state a at time t, $P_a(t)$, is a solution of the master equation. Further mathematical proof is available in elsewhere [58].

Several varieties of the kMC method have been developed. In general, the lattice-based kMC is the most suitable approach when modelling gas-solid reactions that take place on the solid surface [49]. The lattice assumption maps atoms in the system onto sites of a predefined lattice. The locations of all the atoms in the system (system configuration) is a state of the system. An event may move one atom from the its current position to another lattice point, which consequently changes the configuration or the state of the system. This assumption coarse-grains the continuous rapid evolution of adsorbate on the surface to the discrete transition events from state to state. The transition probabilities can be calculated as a function of the current surface configuration and elementary reaction rate constants

obtained from DFT analysis. Therefore, given the rate constants, the kMC algorithm can stochastically propagate the system and make the averaged long-term information about the atomistic model accessible for the macroscale model. The detailed implementation of the kMC algorithm is discussed in Chapter 4.

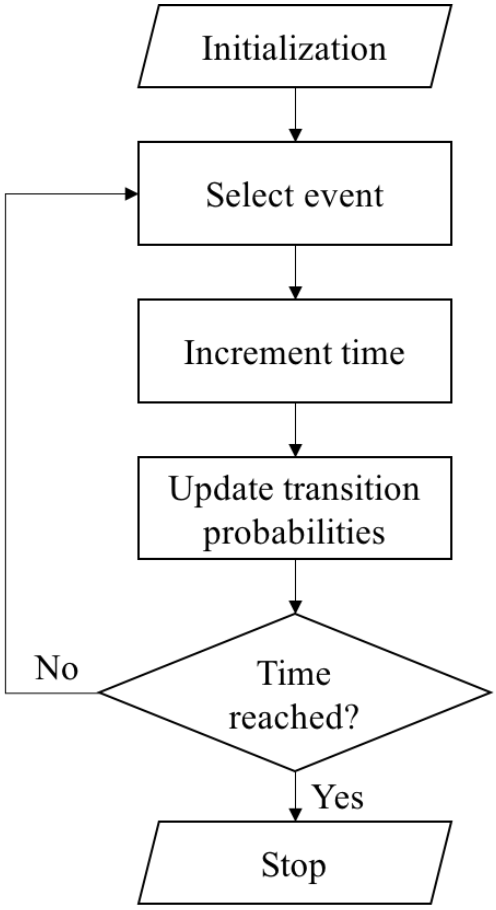

Figure 2.5: kMC algorithm

Model coupling

Given the coarse-grained model, the next step is coupling it with the macroscopic continuum equations that describe the concentration or temperature gradients inside OC particles. The macroscale model is usually a system of ODEs or PDEs solved by numerical methods that discretize the time and spatial domains which are orders of magnitude larger

than events taking place on the the surface area described by the coarse-grained model. Therefore, the reaction rate obtained from the surface model has to be evaluated at all discretization points of the macroscopic domain in order to account for the changes in concentration or temperature. Vlachos *et al.* [59] assessed the numerical feasibility of multi-scale integration hybrid (MIH) algorithms that link a unimolecular surface reaction model to a macroscopic transport model by decomposing the system into two partially overlapping subdomains. Schaefer *et al.* [60] developed a method to couple kinetic Monte Carlo simulations of surface reactions at a molecular scale to transport equations at a macroscopic scale. Other coupling schemes have also been proposed in the past few decades including the hybrid multiscale integration algorithm [61, 62, 63, 64], the equation-free approach [65] and the heterogeneous multiscale method [60, 66]. These techniques have been used to simulate numerous systems such as carbon nanotube growth [67], thin film deposition [68, 69, 70, 71, 72, 73], polymer nanocomposites [74], heterogeneous catalytic flow reactor [75, 76] and dense gas-solid fluidized beds [77]. Reviews on this area are available in the literature [78, 79, 80]. Based on the above, it is clear that coupling models that describe phenomena at different scales is one of the best way to enable top-down optimization in which a predetermined target (*e.g.* increasing selectivity or reactivity) can be achieved by searching for materials with desired electronic properties [81].

This chapter emphasizes the importance of developing an ideal OC particle that remains high reactivity in long-term CLC operations. Having access to a multiscale model can greatly accelerate the development of CLC process. To the author's knowledge, multiscale OC particle model has not been proposed in the literature. Hence, the main objective of this work is to apply the multiscale modelling scheme to OC particles in CLC system and analyse the effect of elementary reactions on the performance of the particle, which may provide new insights that can guide the design of OC particle. The next chapter presents a multiscale OC particle model for a syngas-NiO system featuring the use of a statistical techniques to describe chemical reactions taking place on the interstitial surface and the coupling between macroscale and microscale phenomena.

Chapter 3

Multiscale Model for NiO-based OC Particles

The multiscale model considered in this research comprises a macroscale component, which describes mass transport inside the OC particle and a microscale portion that describes reactions on the particle pore surface. Continuum equations are used to model gas diffusion through the particle pore, whereas mean-field approximation and kinetic Monte Carlo simulations are employed to model the surface reaction at different locations inside the particle. Reaction rate constants used in this model are obtained from DFT simulations, while the ramaining parameters are chosen to be representative of pilot-scale CLC plants [18]. This chapter first illustrates the development of the macroscale and microscale models individually, then explains how they are linked, and lastly presents simulation results and discussion. Part of this work has been published for the ADCHEM 2018 conference [82].

3.1 Model Development

The overall configuration of the multiscale model considered in this study is illustrated in Figure 3.1. The oxygen carrier is considered to be a spherical particle with numerous cylindrical pores. The macroscale model (mass transfer model) describes the process where the fuel gas enters the particle through the inlet of the pores and diffuses in both axial (z) and radial (r) directions. The microscale model (surface reaction model) describes chemical reactions on the surface (*i.e.*, the wall) of the pore. The reaction rates depend on the surface concentrations of fuel gas, the amount of adsorbate on the surface, and the elementary reaction rate constants.

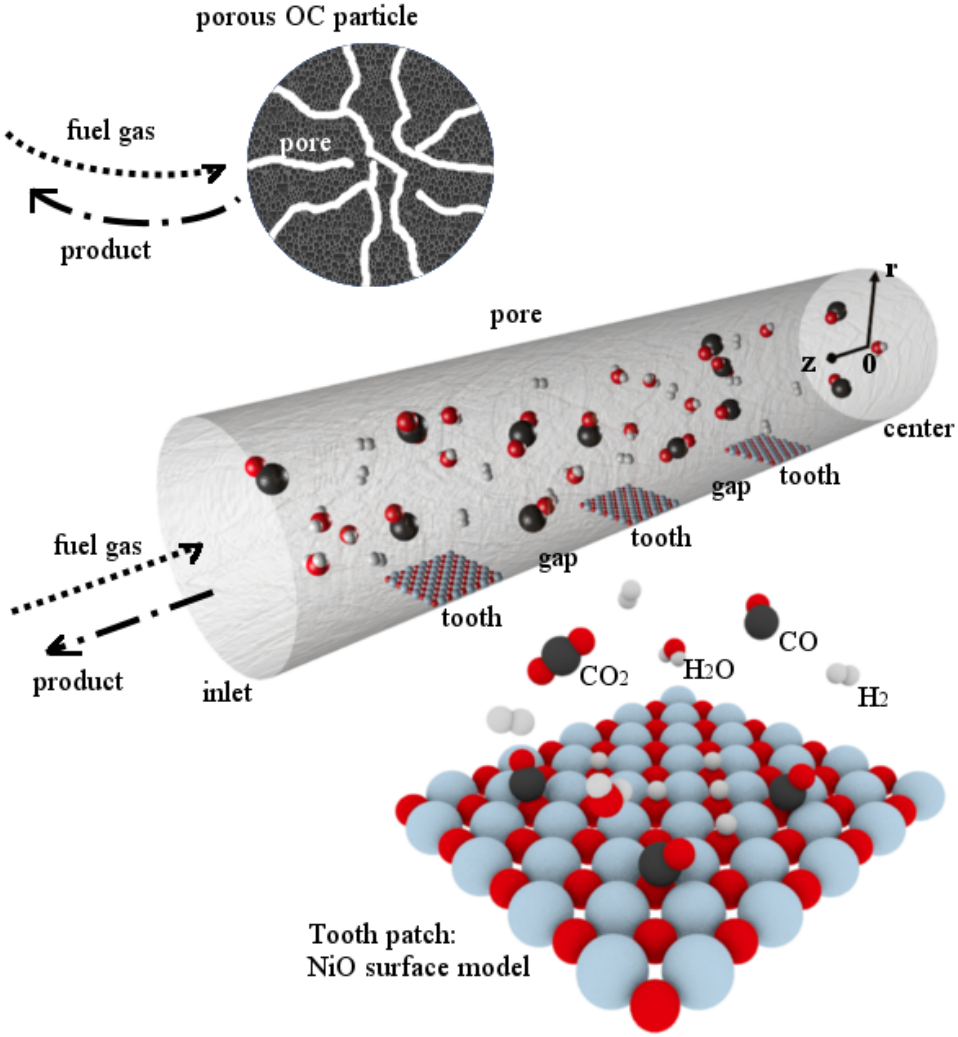

Figure 3.1: Schematic of the present multi-scale model.

When a gas molecule reaches the inner wall of the pore (i.e., boundary in the r-direction), it will either stay on the gas phase or be adsorbed onto the wall surface. The adsorbed molecules will react with the solid reactant on the surface and release the product into the gas phase. The gas concentration profile in the radial and axial directions within the pore is calculated using mass conservation balance equations. The gas phase model and the surface model are coupled through a mass flux boundary condition at the top of the surface, *i.e.*, above the pore's inner walls.

The following assumptions have been adopted in the present model:

1. Structure (*i.e.*, geometry or shape) of the OC particles does not change during the reaction.
2. Isothermal conditions.
3. Mass transport through the particle only occurs by diffusion.
4. Excess oxygen on the pore suface.

3.1.1 Gas Diffusion Model

The two dimensional unsteady-state mass transport of molecules in the gas phase is described by the continuum equation:

$$\frac{\partial C_i}{\partial t} = \mathcal{D}_{e,i}\frac{1}{r}\frac{\partial}{\partial r}\left(r\frac{\partial C_i}{\partial r}\right) + \mathcal{D}_{e,i}\frac{\partial^2 C_i}{\partial z^2}. \tag{3.1}$$

with the following initial and boundary conditions:

$$C_i(t,z,r)\Big|_{t=0} = 0 \tag{3.2}$$

$$\frac{\partial C_i(t,z,r)}{\partial z}\Big|_{z=0} = 0 \tag{3.3}$$

$$\frac{\partial C_i(t,z,r)}{\partial r}\Big|_{r=0} = 0 \tag{3.4}$$

$$-\mathcal{D}_{e,i}\frac{\partial C_i(t,z,r)}{\partial z}\Big|_{z=L} = k_{g,i}\left(C_i(t,z,r)\big|_{z=L} - C_i^{bulk}(t)\right) \tag{3.5}$$

$$-\mathcal{D}_{e,i}\frac{\partial C_i(t,z,r)}{\partial r}\Big|_{r=R} = \mathbf{J}_i(t,z) \tag{3.6}$$

where C_i is concentration of gas i in the pore; r and z are the radial and axial spatial domains; R and L are the pore radius and pore length, respectively; $\mathcal{D}_{e,i}$ is the effective diffusivity of gas i in the pore; $k_{g,i}$ is the external mass transfer coefficient of gas species i; C_i^{bulk} is the bulk concentration of gas i; $\mathbf{J}_i(t,z)$ is mass flux of gas species i above the surface.

There are some variables in the boundary conditions that must be calculated separately. The rate of change of concentration of gas species i in the bulk C_i^{bulk} can be estimated as follows:

$$\frac{dC_i^{bulk}(t)}{dt} = \frac{N_p S_p \mathbf{F_i}|_{z=L}}{V} \tag{3.7}$$

where N_p is the number of particles involved in the reaction; S_p is surface area of a single OC particle; V is the volume of the reacting space; $\mathbf{F_i}|_{z=L}$ is the averaged mass flux of gas i at the inlet of the pore, *i.e.*, the surface of the particle:

$$\mathbf{F_i}|_{z=L} = -\mathcal{D}_{e,i} \frac{\partial C_i(t,z,r)}{\partial z}\bigg|_{z=L} \tag{3.8}$$

accordingly,

$$\frac{dC_i^{bulk}(t)}{dt} = \frac{N_p S_p}{V} k_{g,i} \left(C_i(t,z,r)\big|_{z=L} - C_i^{bulk}(t) \right) \tag{3.9}$$

The effective diffusivity of gas i can be calculated as a function of gas diffusivity and particle porosity as follows:

$$\mathcal{D}_{e,i} = \mathcal{D}_{g,i} \varepsilon^2 \tag{3.10}$$

where ε is the particle porosity. When gas diffuses through the pore, both molecular diffusion and Knudsen diffusion operate. Therefore, the gas diffusivity can be calculated as follows:

$$\mathcal{D}_{g,i} = \left(\frac{1}{\mathcal{D}_{m,i}} + \frac{1}{\mathcal{D}_{K,i}} \right)^{-1} \tag{3.11}$$

The molecular diffusivity $\mathcal{D}_{m,i}$ and the Knudsen diffusivity $\mathcal{D}_{K,i}$ are calculated using the following correlations:

$$\mathcal{D}_{m,i} = \frac{1.0 \times 10^{-7} T^{1.75} \left(M_i^{-1} + M_S^{-1} \right)^{0.5}}{P \left[\left(\sum_i \nu_i \right)^{1/3} + \left(\sum_S \nu_i \right)^{1/3} \right]^2} \tag{3.12}$$

$$\mathcal{D}_{K,i} = \frac{2}{3} r \sqrt{\frac{8RT}{\pi M_i}} \tag{3.13}$$

where T is the particle's temperature in Kelvin; M_i is the molecular weight of gas i; M_S is the molecular weight of the solvent S; P is the pressure in atm; ν_i is the diffusion parameters of the diffusing species i [83].

The external mass transfer coefficient k_g can be calculated using the Sherwood number:

$$k_{g,i} = \frac{\mathcal{D}_{m,i} Sh}{d_{par}} \tag{3.14}$$

where Sh is the Sherwood number; and d_{par} is the particle diameter. Sherwood number represents the ratio between the rate of convective mass transfer to the rate of diffusive mass transport around a spherical pellet. For the typical size of OC particles (0.1 - 0.4 mm), the value of the Sherwood number is approximated to be 2.0 assuming negligible shear stress at the particle outer surface [84].

Lastly, the mass flux of gas species i, $\mathbf{J}_i$, above the surface cannot be directly calculated from the gas diffusion model. Instead, a surface model is required to provide this information. In general, $\mathbf{J}_i$ can be expressed as the mass flux $\mathbf{J}_{i,enter}$ entering the gas phase from the surface minus the mass flux $\mathbf{J}_{i,leave}$ of gas species i leaving the gas phase and adsorbing onto the surface:

$$\mathbf{J}_i(t,z) = \mathbf{J}_{i,enter}(t,z) - \mathbf{J}_{i,leave}(t,z) \tag{3.15}$$

Since the mass flux of CO or H_2 is defined as the rate of molecules leaving the gas phase per unit area, its value depends on the concentration of gas species i, $C_i(t,z,r)\big|_{r=R}$, above the surface, the adsorption rate constant of surface species i, $k_{a,i}$, and the number of available adsorption sites on the surface, $\mathbf{N}_{avail,s}$. The flux of the product gas CO_2 or H_2O depends on the concentration of species i adsorbed on the surface, $C_{i,surface}(t,z)$, and the reaction rate constant of surface species i, $k_{r,i}$. As the macroscale gas diffusion model only contains the value of $C_i(t,z,r)\big|_{r=R}$, other information to calculate the mass flux must be provided by the surface model (microscale model).

3.1.2 Surface Model

The surface or microscale model describes the reactions that take place on the surface, and therefore provides the consumption rate of reactants per unit area as well as the generation rate of products per unit area. To develop a microscale model, the first step is to establish surface reaction mechanism and obtain the corresponding kinetic parameters. There are two approaches to achieve this: one is obtaining them from experimental data, while the other one is calculating them using first-principles methods based on quantum mechanics.

Although laboratory-based kinetic parameters are more reliable, it is usually very difficult to untangle all the elementary reaction steps involved and their corresponding rate constants using only experimental data (*i.e.*, observable macroscale properties). Calculating rate constants theoretically, on the other hand, is generally less accurate. However, it has the significant advantage of providing rate constants of individual reaction steps that are experimentally not accessible.

Given that no experimental data for the studied system is available in the literature, the first-principles calculation is carried out to predict the reaction mechanism and calculate the elementary reaction rate constants, *i.e.*, density functional theory (DFT) simulation using the Vienna Ab Initio Simulation Package (VASP). The projector-augmented wave (PAW) method [85] with the generalized gradient approximation of Perdew-Burke-Ernzerhof [86] is chosen to describe the system. To simulate the reactions, a 6-layer nickel oxide slab model is constructed while the 2 bottom layers are fixed. Through structural relaxation and nudged-elastic-band method [87], we have established the 4-step syngas oxidation mechanism (discussed in the following paragraph) and calculated the rate constants k for all the elementary reactions (See Table 3.1). To obtain the reaction rate constants for this process, we screened multiple configurations and found the most stable structures from DFT analysis for reactants and products in the surface reaction system (details are beyond the scope of this thesis). Transition states of this 4-step-reaction are searched as saddle points, which are confirmed by frequency calculations. The rate constants are calculated using the same temperature (1223K) used in the gas diffusion model. Here, it is important to clarify that all DFT calculations mentioned above are not performed by the author of this thesis. Instead, this work employs part of the preliminary results of a co-worker Yue Yuan's research.

Kinetic Parameters (Units)	Values
H_2 adsorption rate constant, k_{a,H_2} $(M^{-1} \cdot s^{-1})$	8.54
H_2O formation rate constant, k_{r,H_2O} (s^{-1})	3.98×10^{-2}
CO adsorption rate constant, $k_{a,CO}$ $(M^{-1} \cdot s^{-1})$	4.83×10^{-6}
CO_2 formation rate constant, k_{r,CO_2} (s^{-1})	2.79

Table 3.1: Reaction rate constants

Given the set of elementary reactions and their corresponding rate constants, a model can be developed to describe the changes in surface configurations and the rate of surface reactions. As shown in Figure 3.1, the pore surface is considered to be a finite square lattice. Each lattice site can be occupied by at most one molecule through adsorption. According

to the results from the DFT calculations, H_2 molecules are likely to dissociate into two free hydrogen atoms when they approach the surface. The hydrogen atom immediately attach to the exposed oxygen atoms and form a NiO-H micro-structure. Once NiO-H is formed, the bonded O-H can capture a nearby H atom and becomes H_2O. On the other hand, CO molecules tend to attach to the oxygen atoms on the exposed NiO surface and form a NiO-CO micro-structure. After formation of NiO-CO, CO captures the oxygen atom in NiO and becomes CO_2. The energy barriers for NiO-H microstructure formation and CO_2 and H_2O desorption are significantly smaller compared to other reactions and so these steps take place much faster. As a result, it is reasonable to assume that NiO-H microstructure formation and CO_2 and H_2O desorption are not rate-limiting steps and thus, are not considered explicitly in the present model. Therefore, the reaction mechanisms used in the present work involves four steps, as shown in Figure 3.2. These steps are: (i) H_2 molecule dissiciation on the surface, producing two H atoms which occupy two adjacent exposed oxygen atoms (*i.e.*, available adsorption sites) on the surface (Figure 3.2a), (ii) capture of one oxygen among the two adjacent H atoms to become H_2O (Figure 3.2b), (iii) adsorption a CO molecule onto an available site on the surface (Figure 3.2c) and (iv) reaction of the adsorbed CO with NiO to produce CO_2 (Figure 3.2d):

$$\mathrm{H_2(g)} + 2\mathrm{NiO}* \xrightarrow{k_{a,H_2}} 2\mathrm{NiO\text{-}H}* \tag{3.16}$$

$$2\mathrm{NiO\text{-}H}* \xrightarrow{k_{r,H_2O}} \mathrm{NiO}* + \mathrm{Ni}* + \mathrm{H_2O(g)} \tag{3.17}$$

$$\mathrm{CO(g)} + \mathrm{NiO}* \xrightarrow{k_{a,CO}} \mathrm{NiO\text{-}CO}* \tag{3.18}$$

$$\mathrm{NiO\text{-}CO}* \xrightarrow{k_{r,CO_2}} \mathrm{Ni}* + \mathrm{CO_2(g)} \tag{3.19}$$

where $*$ denotes an available adsorption site (*i.e.*, an exposed oxygen atom) on the surface. This work employed the MFA and kMC methods to model the microscale dynamics, as discussed in the following section.

Mean-field Approximation

The most important assumption of the MFA method is that the adsorbed molecules are distributed homogeneously on the surface. The effect of the surface configuration on a single adsorbate is approximated by the average occupancy of lattice sites by any of the adsorbed molecules. For a surface patch located at distance l from the pore inlet ($z = l$), the rate of change of the surface concentration of species i (C_i^{surf}) can be described as the

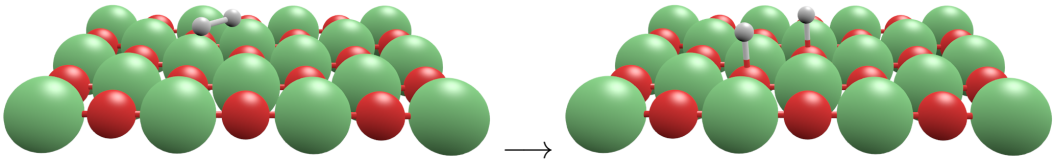

(a) $H_2(g) + 2NiO* \xrightarrow{k_{a,H_2}} 2NiO\text{-}H*$

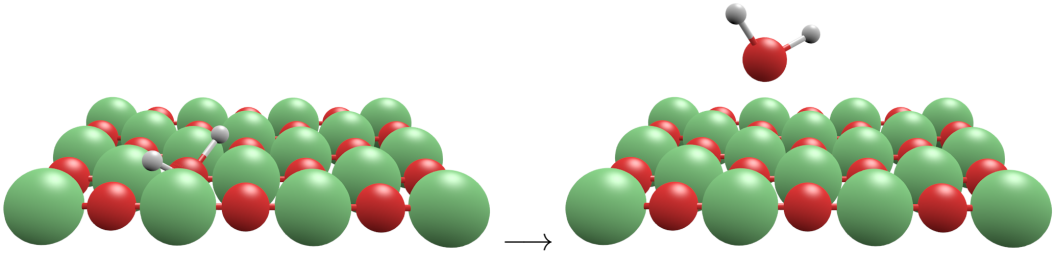

(b) $2NiO\text{-}H* \xrightarrow{k_{r,H_2O}} NiO* + Ni* + H_2O(g)$

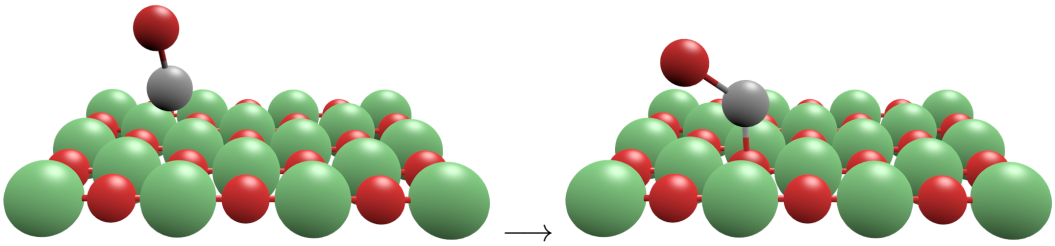

(c) $CO(g) + NiO* \xrightarrow{k_{a,CO}} NiO\text{-}CO*$

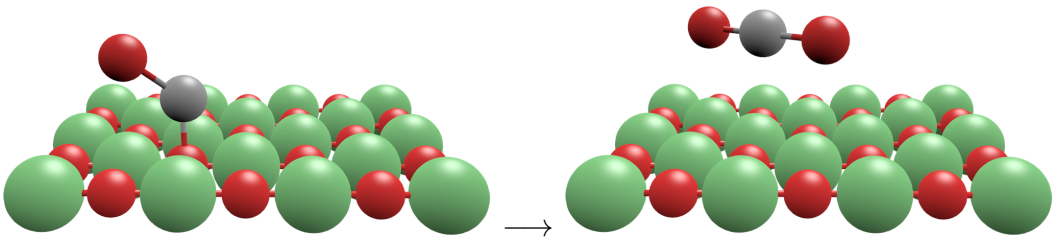

(d) $NiO\text{-}CO* \xrightarrow{k_{r,CO_2}} Ni* + CO_2(g)$

Figure 3.2: Elementary reactions

rate of adsorption minus the rate of consumption:

$$\frac{\partial C_i^{surf}(t,l)}{\partial t} = k_{a,i} C_i^{gas}(t,z,r)\big|_{z=l,r=R} C_{vac}^{surf}(t,l) - \sum_{n=1}^{n_r} k_{r,i,n} C_i^{surf}(t,l) \tag{3.20}$$

where $C_i^{gas}(t,z,r)\big|_{z=l,r=R}$ is concentration of gas i above the surface ($r = R$) located at distance l from the pore entrance, and is estimated in the gas phase model; $C_{vac}^{surf}(l,t)$ is the surface concentration of vacant adsorption site; $C_i^{surf}(l,t)$ is surface concentration of species i; n_r is the number of reactions that consume species i and $k_{r,i,n}$ is the reaction rate constant for these reactions.

Equation 3.20 can also be expressed in terms of the surface coverage fraction as follows:

$$\frac{\partial \theta_i(t,l)}{\partial t} = k_{a,i} C_i^{gas}(t,z,r)\big|_{z=l,r=R} \left(1 - \sum_{j=1}^{n_s} \theta_j(t,l)\right) - \sum_{n=1}^{n_r} k_{r,i,n} \theta_i(t,l) \tag{3.21}$$

where n_s is the number of surface species (as discussed in Section 3.1.2, surface species in this model are adsorbed CO and H; hence, $n_s = 2$ in this framework); and θ_i is surface coverage fraction of species i.

The following constraint is added to ensure mass species conservation:

$$1 = \theta_{vac}(t,l) + \sum_{i=1}^{n_s} \theta_i(t,l) \tag{3.22}$$

For the proposed reaction mechanisms described in Section 3.1.2, the following equations are considered in the present surface model:

$$\frac{\partial \theta_{CO}(t)}{\partial t} = k_{a,CO} C_{CO}(t,z,R) \theta_{vac}(t,z) - k_{r,CO} \theta_{CO}(t,z) \tag{3.23}$$

$$\frac{\partial \theta_H(t)}{\partial t} = 2k_{a,H_2} C_{H_2}(t,z,R) \theta_{vac}^2(t,z) - 2k_{r,H_2} \theta_H^2(t,z) \tag{3.24}$$

$$1 = \theta_{vac}(t,z) + \theta_{CO}(t,z) + \theta_H(t,z) \tag{3.25}$$

The present mechanism assumes that the oxygen on the surface is in excess during the time period in the simulation and the CO_2 and H_2O molecules leave the surface immediately after they are produced. Hence, CO and H_2 molecules always have access to oxygen atoms (Assumption 3) and no CO_2 or H_2O molecule will remain on the surface because of the fast desorption of CO_2 and H_2O compared to other reactions (the surface coverages of CO_2 and H_2O are always zero).

The mass flux $\mathbf{J}$ for each gas species at a distance l from the pore inlet in the z-direction is calculated as follows:

$$\mathbf{J}_{CO}(t,z)\big|_{z=l} = -\frac{C_s}{N_A} k_{a,CO} C_{CO}(t,z,r)\big|_{z=l,r=R} \theta_{vac}(t,z)\big|_{z=l} \tag{3.26}$$

$$\mathbf{J}_{CO_2}(t,z)\big|_{z=l} = \frac{C_s}{N_A} k_{r,CO} \theta_{CO}(t,z)\big|_{z=l} \tag{3.27}$$

$$\mathbf{J}_{H_2}(t,z)\big|_{z=l} = -\frac{C_s}{N_A} k_{a,H_2} 2C_{H_2}(t,z,r)\big|_{z=l,r=R} \theta^2_{vac}(t,z)\big|_{z=l} \tag{3.28}$$

$$\mathbf{J}_{H_2O}(t,z)\big|_{z=l} = \frac{C_s}{N_A} k_{r,H_2} \theta^2_{H}(t,z)\big|_{z=l} \tag{3.29}$$

Here, C_s is surface site density and N_A is the Avogadro constant. The constant $\frac{C_s}{N_A}$ represents surface site density in units of mole per square meter, which is also the concentration of surface species when its coverage reaches 100%. Note that $\mathbf{J}_i$ is also the mass flux term in the boundary condition of gas diffusion model (Eq.3.6), and the value of CO and H_2 concentration in the gas phase is required to solve the surface model.

Kinetic Monte Carlo

The microscale model describing surface reactions using mean-field approximation neglects the effect of lateral interactions (interactions between adsorbates). For example, the adsorption on an isolated vacant adsorption site typically happens much faster than the adsorption on an vacant adsorption site surrounded by adsorbates due to the presence of repulsive forces between atoms and molecules. Thus, the rate constants of elementary reactions are dependent on the nearby surface configurations of the reacting site. Kinetic Monte Carlo method is capable of simulating lateral interactions and incorporating the dependence of rate constants on surface configurations properly, which makes it suitable to interpret the results from DFT simulations. In the present surface model, the reacting surface is modelled as a N by N square lattice with periodic boundary conditions. Each point on the lattice represents an active site (or an exposed oxygen atom). The lateral interactions are described as follows:

- The reactant rate constants on a lattice site can only be affected by its first nearest neighbors, which are the adjacent lattice sites on its front, back, left, right direction (four in total).

- The dissociative adsorption of H_2 molecule occupies two adjacent oxygen atoms. Therefore, if an empty site does not have at least one available site as its first nearest neighbour, it does not allow H_2 adsorption to occur.

- Adsorbate changes the elementary reaction rate constants on its nearby sites due to intermolecular interactions. In order to accurately account for the effect of nearest neighbors, more detailed DFT simulations are required. For instance, the adsorption of CO molecules can be categorized into 15 scenarios: adsorption on an isolated empty site; adsorption on an empty site with one/two/three/four adjacent adsorbed CO; adsorption on an empty site with one/two/three/four adjacent adsorbed H; adsorption on an empty site with nearest neighbors that are one CO and one H, one CO and two H, two CO and one H, three H and one CO, three CO and one H, as well as two CO and two H. Similar simulations must also be conducted for H_2 adsorption. At this moment, results from the mentioned DFT simulations are not available. Therefore, kMC simulation assumes that the presence of one CO adsorbate decreases the adsorption rate on its adjacent site by 20%, whereas the presence of one H adsorbate decreases the adsorption rate on its adjacent site by 10%. The effect of nearest neighbors is also assumed to be increasing exponentially. Thus, when one empty site has two adsorbed CO neighbors, the adsorption rates of both H_2 and CO are lowered by 36%. Here, it is necessary to clarify that all the assumptions made when counting nearest neighbor effect are educated guesses, but they can easily be modified once more information from DFT simulations becomes available.

Similar to the MFA-based surface model, the present kMC-based surface model takes the gas phase concentration of CO and H_2 as the input, and provides the value of mass flux $\mathbf{J}_i$ at each kMC patch as the output. Before starting the kMC simulation, it is essential to determine a list of all possible events that can be realized during the simulation. In this work, the events considered are: (1) CO adsorption; (2) H_2 dissociative adsorption; (3) CO$*$ (adsorbed CO) reaction; and (4) H$*$ (adsorbed H) reaction (See Figure 3.2). The kMC algorithm implemented in this work is shown in Figure 3.3 and is summarized as follows:

1. Generate an initial configuration based on the input parameters and set the internal timer τ to zero. The input parameters are the concentrations of CO and H_2 above

the surface (C_{CO}^{gas} and $C_{H_2}^{gas}$), the simulating time period τ_f, which is equal to the time increment dt used to solve gas diffusion PDE, and the final surface configuration from the previous simulation $\mathbf{S}_{old}$. The initial surface configuration is set to be the same as $\mathbf{S}_{old}$. If the current simulation is the first one, an empty lattice is generated to represent a clean NiO surface.

2. Calculate the probability of CO and H_2 adsorption events as:

$$W_{a,i,n} = aC_i(t, l, R)k_{a,i}N_n f \tag{3.30}$$

where $W_{a,i,n}$ is the probability of gas species i (CO or H_2) adsorption on an empty site that has n nearest neighbors (n = 0, 1, 2, 3,or 4); a is stoicheiometry number in elementary reaction ($a = 1$ for CO; $a = 2$ for H_2); N_n is the number of empty lattice sites with n nearest neighbor(s); f represents the overall effect of lateral interaction; $k_{a,i}$ is the adsorption rate constant; $C_i(t, l, R)$ is the concentration of gas species i above the surface located at distance l from the pore inlet, which is determined by the gas diffusion (macroscale) model.

3. Calculate the probability of CO$*$ and H$*$ reaction events as follows:

$$W_{r,j} = N_j k_{r,j} \tag{3.31}$$

where $W_{r,i}$ is the probability of adsorbate j (CO$*$ or H$*$) reacting with an exposed oxygen atom to form the product; N_j is the number of lattice sites occupied by adsorbate j; and $k_{r,i}$ is the reaction rate constant of elementary reaction.

4. Calculate the total probability W_{tot} by adding the probabilities of all possible surface events:

$$W_{tot} = \sum_{i,n} W_{a,i,n} + \sum_{j} W_{r,j} \tag{3.32}$$

Generate a standard uniformly distributed random number ξ_1; select the event q that fulfills the condition:

$$\sum_{i=1}^{q-1} W_i \leq \xi_1 W_{tot} \leq \sum_{i=1}^{q} W_i \tag{3.33}$$

5. Execute event q on the surface, that therefore changes the surface configuration. For instance, when H_2 dissociative adsorption on an vacant site with one neighbor (can either be CO$*$ or H$*$) is selected, the simulation will then randomly choose one lattice site from all eligible sites as well as one of the adjacent vacant sites and change their

occupancies from available for adsorption to occupied by H. As a result, these two sites are no longer eligible for any adsorption event, but instead become eligible for a H$*$ reaction event. On the other hand, when H$*$ reaction, is selected, the simulation will randomly select two adjacent sites occupied by H and change their occupancies from occupied by H to available for adsorption. Consequently, no reaction can take place on these two sites, and they become eligible for adsorption events.

6. Generate another standard uniformly distributed random number ξ_2 and advance the internal timer τ by:

$$\Delta\tau = -\frac{ln\xi_2}{W_{tot}} \tag{3.34}$$

7. Repeat Step 2-6 until the internal timer τ reaches the required simulating time period τ_f.

During the kMC simulation, the number of occurrences of both adsorption and reaction events are tracked by different counters. At the end of each simulation (*i.e.*, once τ_f is reached), mass flux of gas phase species i at distance l in axial direction from the pore inlet is obtained through the following formula:

$$\mathbf{J}_i\big|_{z=l} = \frac{\eta_i}{N_A A_s \tau_f} \tag{3.35}$$

where $\mathbf{J}_i\big|_{z=l}$ is the mass flux of gas i at distance l in the axial direction from the pore inlet, η_i is the number of molecule i adsorbed on or released from the surface, N_A is the Avogadro constant and A_s is the area of the simulated surface.

3.1.3 Model Coupling

In the present work, the implicit backward Euler discretization has been employed to solve the macroscale gas diffusion model, whereas the gap-tooth method [88] is adopted to compute the concentration gradients across the pore axial domain. As shown in Figure 3.4, the tooth represents the surface model placed at equally-spaced discrete points in the z-direction of discretized the two-dimensional spatial domain, whereas the gap is a series of discrete points between two subsequent teeth (i.e. surface models). This coupling scheme is based on the interaction between the gas diffusion model and the surface model - the concentration of gas species i above the surface affects the surface configuration through the adsorption term, which in turn affects the adsorption and reaction rates that determine the boundary condition of the gas diffusion model.

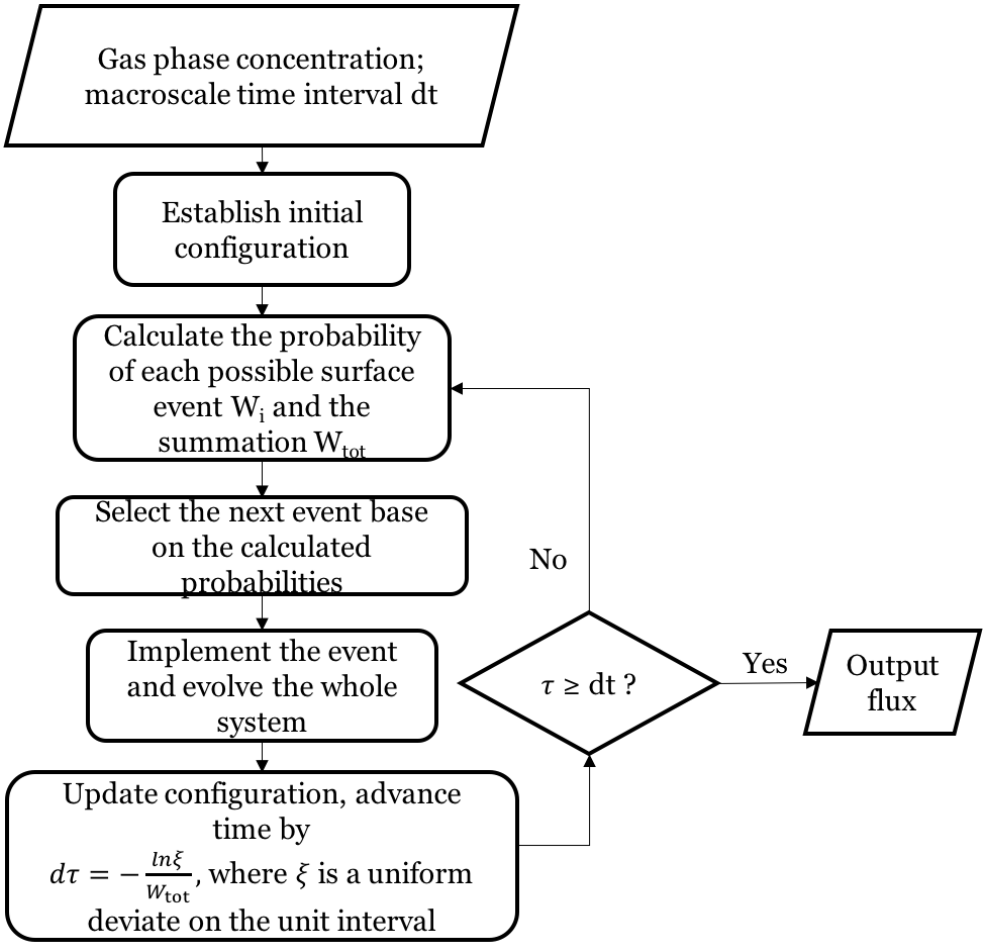

Figure 3.3: KMC algorithm in the present multi-scale model.

The number of teeth points required to solve the model is problem-specific. The present work uses ten teeth to obtain a trade-off between numerical accuracy and computational cost. The multiscale simulation begins by solving the macroscale model (gas diffusion model described by PDEs) to obtain the concentration profile inside the pore at time $t = dt$; the concentration of gas species i at that tooth point $C_i(t, r, z)\big|_{t=dt, z=l_{tooth}, r=R}$ as well as the time interval dt are then passed down to the surface model to calculate the mass flux of molecule i at that specific node (l_{tooth}, R), which is required to evaluate the gas phase boundary condition (Eq.3.6) and solve the macroscale model (Eq.3.1) for the next time interval. Note that surface models are only simulated at ten teeth nodes. MFA-based surface models provide the coverage $\theta_i\big|_{t=dt}$ of surface species i, which is then interpreted as mass flux $\mathbf{J}_i$ (Eq.3.26 to 3.29), at every tooth node. On the other hand, kMC-based surface models directly provide the mass flux $\mathbf{J}_i$ (Eq.3.35) at every tooth node. A linear interpolation function is employed to calculate the value of mass flux $\mathbf{J}_i$ at discrete points between two teeth points provided the results from surface models at teeth located in both ends of the gap. Given the boundary condition, macroscale model updates the concentration profile, and the PDE-(MFA/kMC) loop continues until it reaches the final integration time defined by the user.

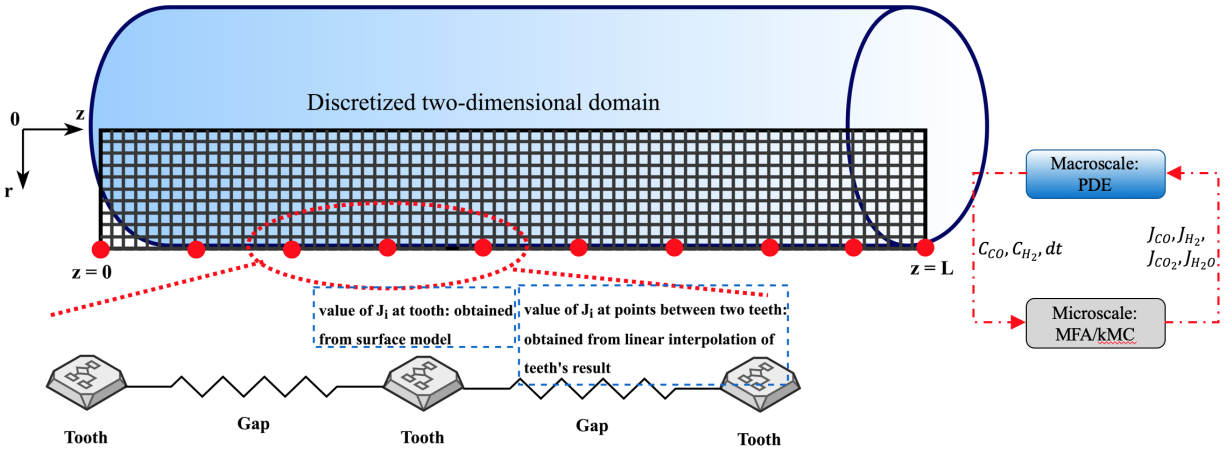

Figure 3.4: Schematic of the gap-tooth method

Parameters (Unit)	Values
Temperature, T (K)	1223
Pressure, P (atm)	1
Particle radius (Pore length), L (m)	1.0×10^{-4}
Pore radius, R (m)	1.0×10^{-8}
Porosity, ε	0.36
Molecular Diffusivity of CO, $\mathcal{D}_{m,CO}$ $(m^2 \cdot s^{-1})$	2.44×10^{-4}
Molecular Diffusivity of CO_2, $\mathcal{D}_{m,CO_2}$ $(m^2 \cdot s^{-1})$	1.93×10^{-4}
Molecular Diffusivity of H_2, $\mathcal{D}_{m,H_2}$ $(m^2 \cdot s^{-1})$	9.25×10^{-4}
Molecular Diffusivity of H_2O, $\mathcal{D}_{m,H_2O}$ $(m^2 \cdot s^{-1})$	3.05×10^{-4}
Effective Diffusivity of CO, $\mathcal{D}_{e,CO}$ $(m^2 \cdot s^{-1})$	8.10×10^{-7}
Effective Diffusivity of CO_2, $\mathcal{D}_{e,CO_2}$ $(m^2 \cdot s^{-1})$	6.46×10^{-7}
Effective Diffusivity of H_2, $\mathcal{D}_{e,H_2}$ $(m^2 \cdot s^{-1})$	3.03×10^{-6}
Effective Diffusivity of H_2O, $\mathcal{D}_{e,H_2O}$ $(m^2 \cdot s^{-1})$	1.01×10^{-6}
Density of sites, C_s $(sites \cdot m^{-2})$	1.33×10^{19}
Syngas concentration, C_0^{bulk} (mM)	300
Sherwood number, Sh	2

Table 3.2: Model Parameters

3.2 Results and Discussion

The multiscale model presented in the previous section was implemented in Python 3.6; Each simulation requires approximately 590 CPU seconds using the MFA-based model and 775 seconds using the kMC-based model (2.5GHz Intel i7-4710MQ processor). The spatial domain is discretized into 21 points in the z-direction and 6 points in the r-direction. Ten surface models are placed equidistantly in the z-direction (See Figure 3.4). Table 3.2 shows the parameters used in this study. The surface site density C_s was published by [89] whereas the operating conditions were taken from [90]. These conditions are representative of pilot-scale CLC plants.

The OC particle model is placed in a closed volume that is initially full of syngas and nitrogen, which represents the sample holder in the TGA experiment conducted by Abad *et al.* [90]. During the simulation, the volume fraction of CO and H_2 in the closed space decreases while the volume fraction of product gas CO_2 and H_2O increases due to the effect of mass transfer and chemical reactions inside the OC particle. Experimental results that can be used to directly compare with the simulation results are not available at the

moment. However, the changes in vol% of gas species can be interpreted as the rate of reactant consumption and product generation, and are therefore used as the reference for the system behavior. Note that the assumption of excess oxygen on the surface is not valid for a process that reaches complete conversion of the OC particle. In reality, as more and more oxygen carried by OC is consumed, available oxygen atoms on the pore surface become more scarce. Since a full conversion of OC particle typically needs 20-60 seconds [9], the simulation is only performed for the first 10 seconds of the reaction to assure that the assumption of excess oxygen remains valid.

As shown in Figure 3.5, MFA-based (represented by dashed lines) and kMC-based (represented by solid lines) models have produced similar qualitative results that agree with the rate of solid conversion of OC particle measured in the experiment [90] (represented by solid dots). In the experiment, the solid conversion was measured as the ratio of the weight loss of reacted OC particles to the initial weight of fresh particles. As the oxygen carried by the solid particle transfers into the reaction products (CO_2 and H_2O), the solid conversion is related to the volume percentage of the product gas. The fastest solid conversion was achieved when the syngas contains 5% CO and 20% H_2, followed by a syngas that contains 30% CO and 5% H_2. Lastly, the experiment using 15% CO and 5% H_2 syngas showed the lowest solid conversion in all the cases tested. Similarly, the simulation results obtained using 5% CO and 20% H_2 syngas shows the highest product gas vol % whereas the 30% CO and 5% H_2 mix resulted in the second highest; in addition, the 15% CO and 5% H_2 syngas mix resulted in a product gas vol % that is significantly lower than the former two cases. Note that the kMC-based model exhibited higher sensitivity to the changes in fuel gas compositions, whereas the MFA-based model is relatively insensitive to changes in the inlet gas compositions. This can be explained by the effect of lateral interactions. Because H_2 adsorption has a reaction rate constant that is six orders of magnitude larger than that of CO adsorption, NiO surface quickly becomes covered by H atoms regardless of the CO to H_2 ratio. According to the MFA-based model, once the surface is almost fully occupied, the rate of H_2O formation turns into the rate limiting step. Since the rate constant for H_2O formation, k_{r,H_2O}, is two orders of magnitude smaller than the rate constant for H_2 adsorption, the increases in H surface coverage θ_H due to H_2 adsorption quickly makes up for the drop in θ_H due to the consumption of the adsorbed H. Consequently, MFA-based model showed little response to the 15% increment in CO composition (the red dashed line overlaps with the blue dashed line), whereas the 15% increment in H_2 composition only increased the product gas generation by a narrow margin. In the kMC simulation, on the other hand, two adjacent available sites are required for H_2 dissociative adsorption event to happen. Thus, if an empty lattice site is surrounded by four occupied neighbors, the only possible event that can take place on that particular site is CO adsorption. Therefore,

although H_2 adsorption has the fastest reaction rate in the system (hence, it has the highest probability to happen), once no adjacent available sites remain, only two possible events can occur: H_2O formation or CO adsorption. This restriction makes CO adsorption much more likely to occur on the surface, which consequently makes the number of adsorbed CO molecules more sensitive to the changes in CO composition of the fuel gas. Since CO_2 formation has higher reaction rate constant (four orders of magnitude times larger than H_2O formation), CO_2 formation is likely to occur as long as CO adsorbs. Hence, when the CO composition increases by 15%, the product gas composition also varies significantly (the blue solid line is clearly higher than the red solid line as shown in Figure 3.5).

Although the experiment data required for a direct comparison is not available, it is clear from the simulation results that the proposed multiscale model underestimates the overall reaction rate. This behavior is likely caused by the kinetic parameters used in the model. As shown in Table 3.2, the adsorption rate for H_2 is eight orders of magnitude larger than the adsorption rate of CO. On the contrary, the reaction rate of adsorbed CO is four orders of magnitude times larger than that of adsorbed H. As a result, the surface is quickly populated with H and almost every CO molecule remains in the gas phase due to the lack of available adsorption sites. Despite being a dominant surface species, the reaction rate of adsorbed H is very small. On the other hand, the faster reaction (*i.e.*, CO oxidation) also becomes a rare event because CO molecules have difficulty adsorbing on the surface to react with the exposed oxygen atoms. As mentioned in Section 2.5, kinetic parameters for the system of study are provided by TST and DFT analysis. Consequently, the accuracy of the multiscale model is also limited by the accuracy of methods used to search for the transition states and parameterize the reaction rate constants. Despite their widespread popularity and success, these methods have their limitaions and can sometimes fail to predict reaction kinetics due to the assumptions, approximations and uncertainties associated with these parameters [80, 91, 92, 93]. Moreover, for the multiscale model, a small error in the rate constant can be magnified and cause large deviations in the macroscale behavior.

3.3 Sensitivity Analysis

Because of the scarcity of similar OC particle models and comparable experimental data, a detailed model validation cannot be performed at this time. Therefore, we carried out a sensitivity analysis on the key modelling parameters to evaluate their effects on the system behaviour. Accordingly, the sensitivity of the multi-scale model to the kinetic parameters

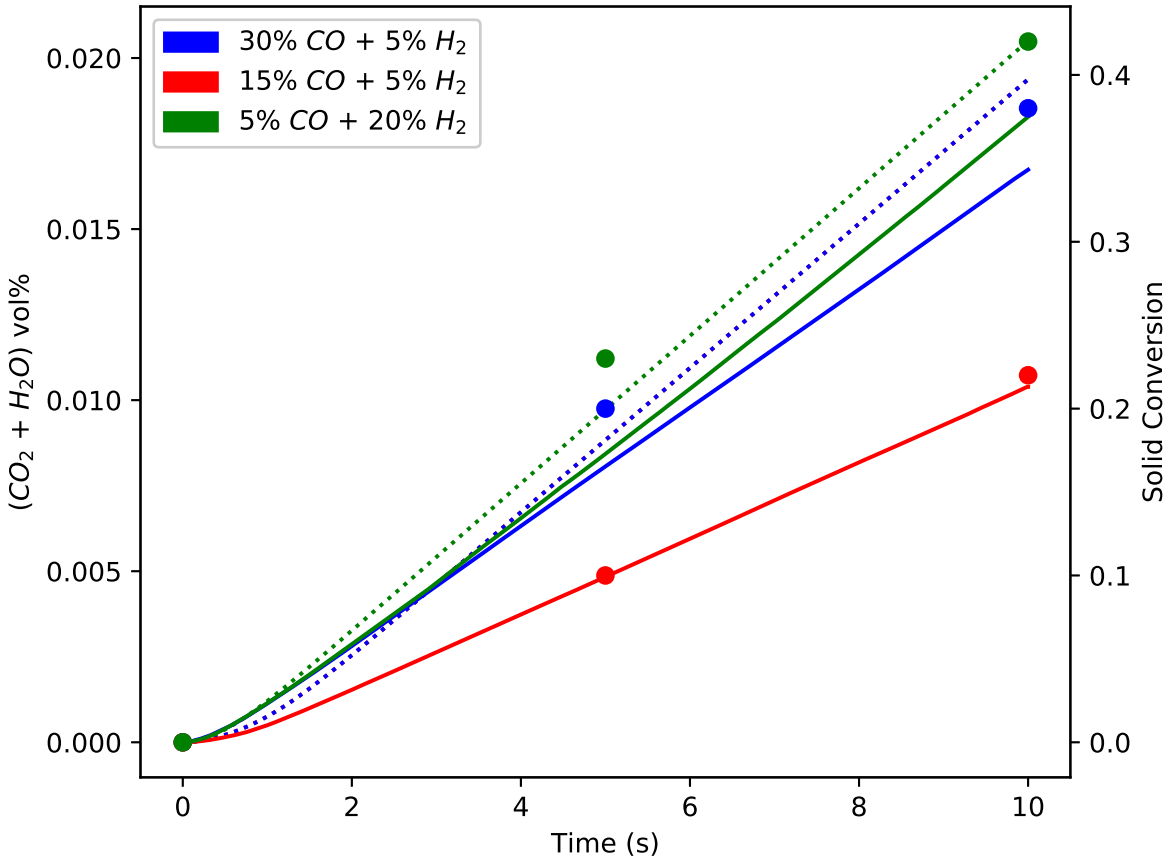

Figure 3.5: Qualitative comparison between simulation results and experimental data using different syngas compositions.

(Simulation results from kMC-based and MFA-based models are represented by solid and dashed lines, respectively. (Note that the red dashed line is missing because it overlaps with the blue dashed line). Experimental data is illustrated in the y-axis on the right-hand side by solid dots.)

was evaluated by changing each kinetic parameter by 10^{-3} and 10^{3}. As shown in Figure 3.6, $k_{r,H}$ has the largest impact on the product gas vol% followed by $k_{a,CO}$. These results support the explanation of slow overall reactions observed in Figure 3.5.

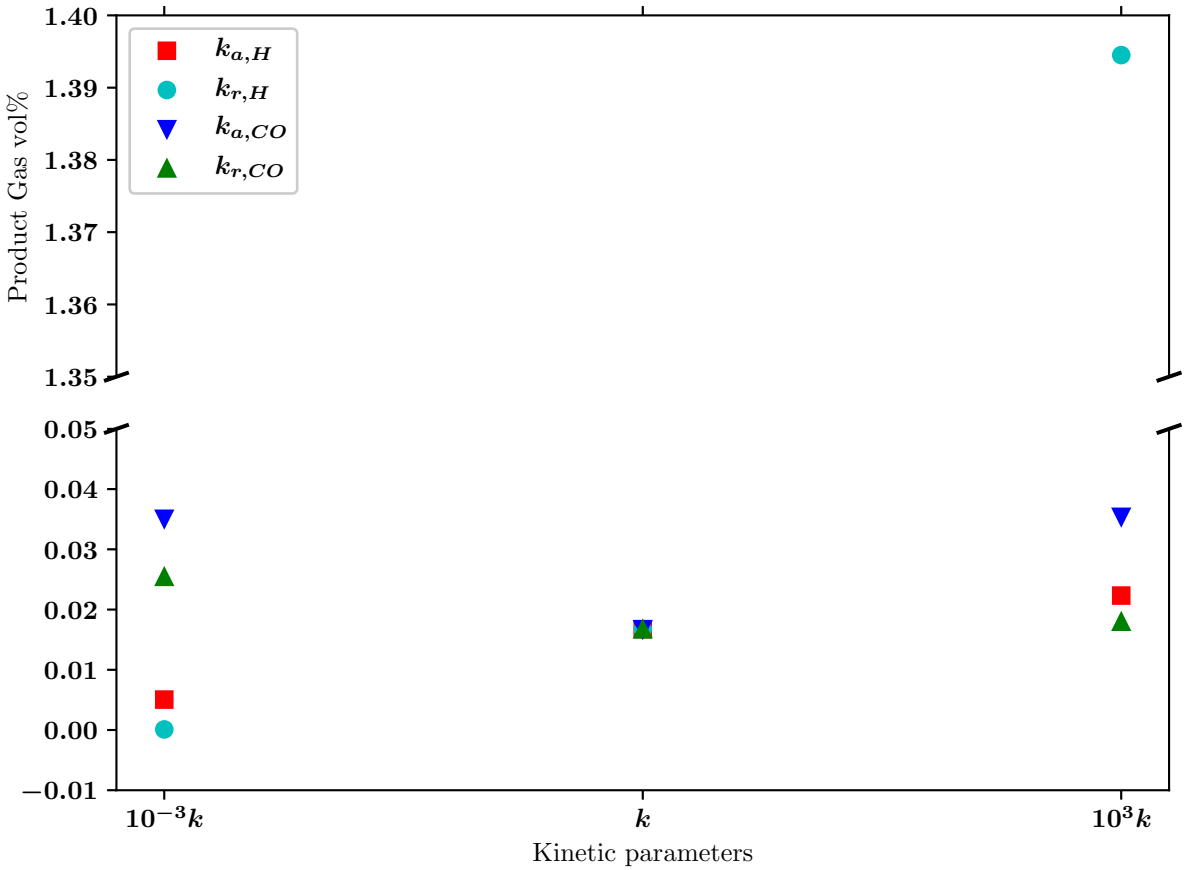

Figure 3.6: Sensitivity analysis: kinetic parameters

According to the results shown in Figure 3.5 and 3.6, the reaction rate inside the OC particle is controlled by the kinetic parameters used in the microscale model. Consequently, the effect of the remaining modelling parameters cannot be explicitly quantified. In order to assess the effect of the remaining modelling parameters and also test the performance of the proposed multiscale model when using different sets of reaction kinetic parameters, a new set of reaction rate constants was used for the sensitivity analysis presented in the following sections. As shown in Table 3.3, k_{r,H_2} and $k_{a,CO}$ are modified to match the order of k_{a,H_2} and $k_{r,CO}$. These two rate constants were chosen because they are likely causing

the low overall reaction rates. Similar values have also been used in other multiscale models in terms of orders of magnitude. As shown in Figure 3.7, the modified parameters have significantly increased the generation of product gases (H_2O and CO_2). The MFA-based model predicted faster generation rate in all three cases. This disagreement is caused by the effect of lateral interactions considered in the kMC-based model: adsorbates prevent molecules from attaching to surrounding surface sites. This effect has a greater influence on H_2 dissociative adsorption that requires two available adjacent sites. Consequently, the largest difference between the kMC-based and MFA-based models is observed at the highest H_2 composition in the fuel gas (20%).

Parameters	Values
k_{a,H_2}	8.54
k_{r,H_2}	3.98
$k_{a,CO}$	4.85
$k_{r,CO}$	2.79

Table 3.3: Modified Kinetic Parameters

The rates of the reactions inside the OC particle depends on several factors such as the physical properties of the particles (particle size, porosity, composition, *etc.*) and chemical kinetics of the reactions. The next sections present the sensitivity analysis of the kMC-based model to the length of the pore (or the size of the OC particle) and the porosity of the solid particle. The results were generated using surface models solved equidistantly at 10 positions along the length of the pore. The surface is represented as a 64×64 lattice as the trade-off between computational time (see Table 3.4) and fluctuations in the simulation results caused by the stochastic nature of kMC simulations (see Figure 3.8). Although using the 64×64 lattice increases the averaged simulation time by 1,100 seconds compared to the 32×32 lattice, it also reduces the stochastic fluctuations significantly. On the other hand, the results obtained from the 128×128 lattice show the least fluctuation, but compared to the simulation results using 64×64 lattice, the improvement is not substantial enough to justify the extra 5,100 seconds in computational time. The parameters presented in Table 3.2 and 3.3 are considered as the base case for the sensitivity analysis. The fuel gas composition considered in the analysis is 30% CO and 5% H_2.

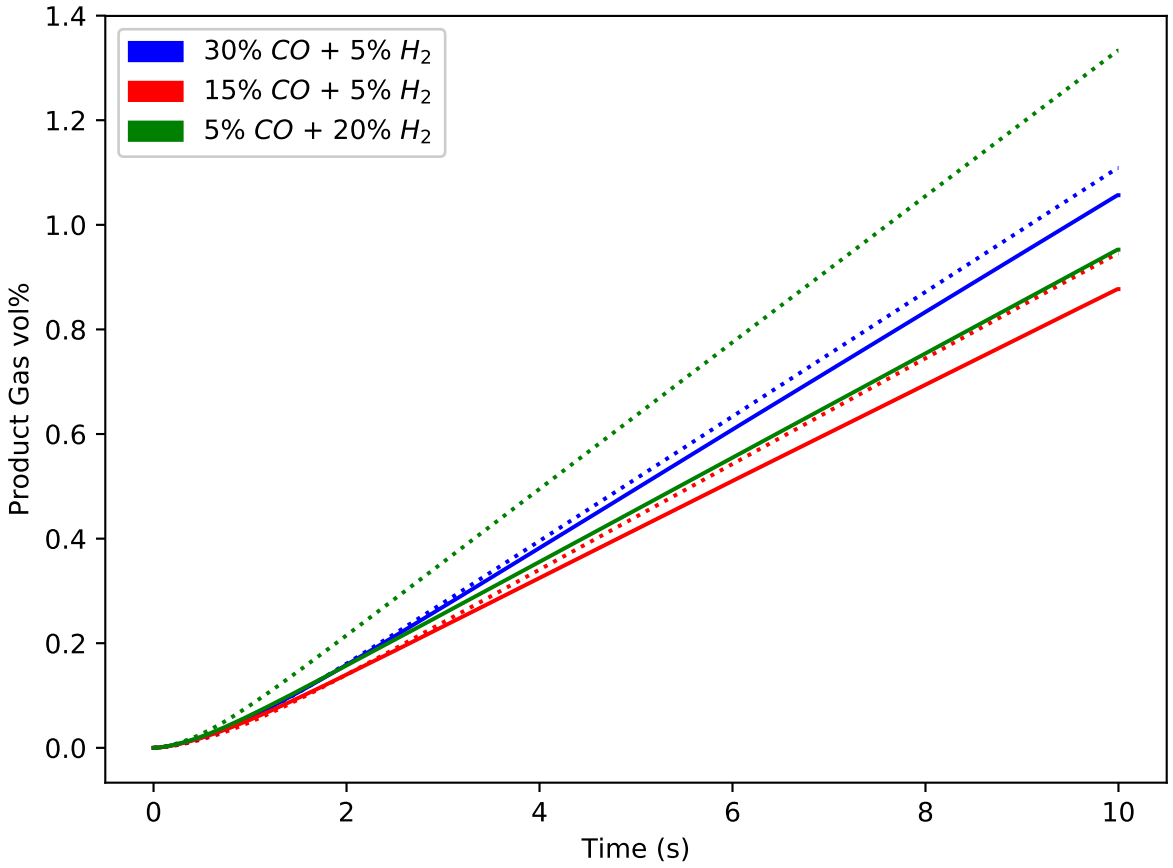

Figure 3.7: Simulation results using modified kinetic parameters. Results from kMC-based and MFA-based models are represented by solid and dashed lines, respectively.

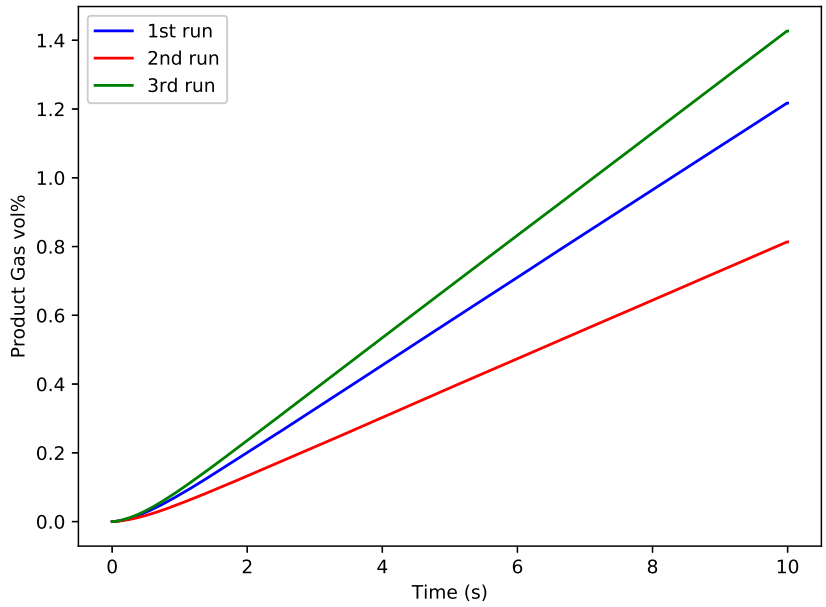

(a) 32×32

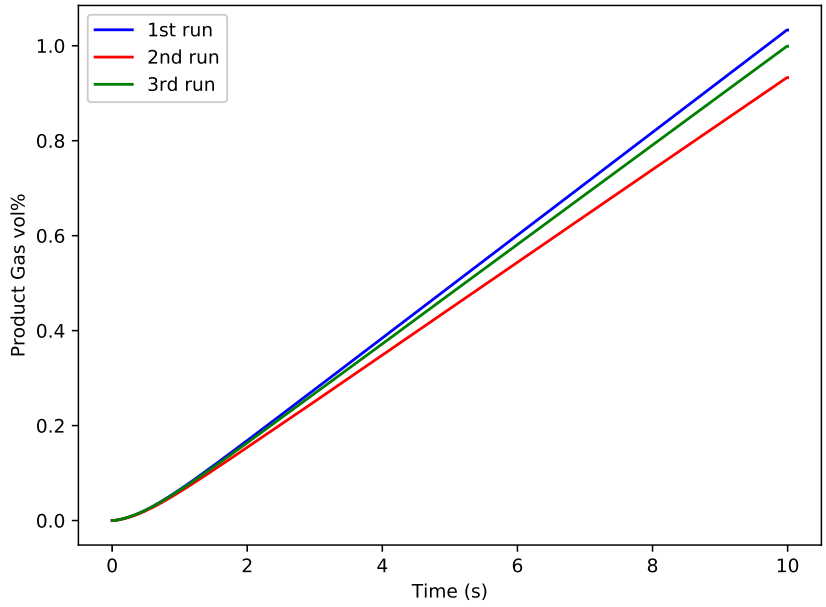

(b) 64×64

Figure 3.8: Repeated simulation results using different lattice sizes.

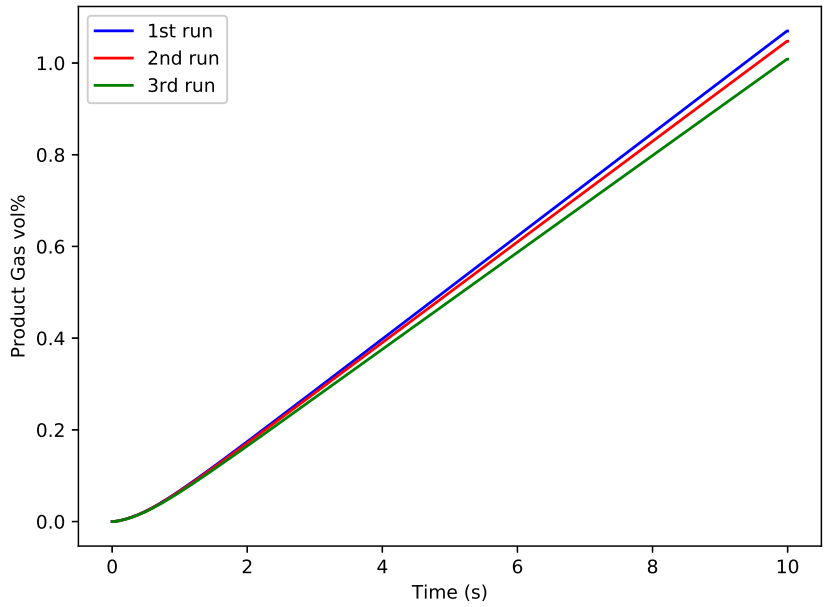

(c) 128 × 128

Figure 3.8: Repeated simulation results using different lattice sizes.

Lattice size	CPU Time (s)
32×32	1,300
64×64	2,400
128×128	7,500

Table 3.4: Averaged Simulation Time

Effect of the pore length

Figure 3.9 shows the impact of pore length on the generation rate of product gas (CO_2 and H_2O). The evolution of product gas leaving the pore (*i.e.*, the exterior surface of the OC particle) was simulated using +/- 20% changes in the pore length (*i.e.*, size of the particle). The result shows that the generation rate of product gas in a larger particle is higher than that obtained from a smaller particle. This behavior is expected because increasing pore length increases the path of gas diffusion and the available solid reactant content, thus enhancing both fuel gas adsorption and the adsorbate reaction processes.

Furthermore, the profile of surface coverage of CO and H at equally-spaced teeth points in the axial direction was evaluated after each simulation. As shown in Figure 3.10, the surface coverage of CO at the inlet of the pore was higher than that at the end of the pore whereas the coverage of H showed the opposite tendency. This is because CO concentration is higher at the inlet (30%) while H_2 has higher diffusivity and adsorption rate constant. Moreover, in the simulation with + 20% pore length, the fuel gas did not reach the center of the particle by the end of the simulation, as suggested by the zero surface coverages for both species at the point where pore length equals zero. This means that the speed of gas diffusion through the pore also plays a role in the overall reaction process.

Effect of the particle porosity

Changing the particle porosity directly changes the effective diffusivities for all gas species. Table 3.5 and 3.6 show the new effective diffusivities calculated by Eq.3.10. Increasing particle porosity promotes the gas diffuision process. As shown in Figure 3.11, higher product gas vol% was achieved in the simulation using + 20% porosity; on the other hand, the - 20% porosity resulted in lower product generation compared to the base case condition. This result is reasonable because faster gas diffusion increases the number of fuel gas molecules above the pore surface, which increases the probabilities of adsorption onto the surface (Eq.3.30). Events with high probabilities are executed frequently in kMC

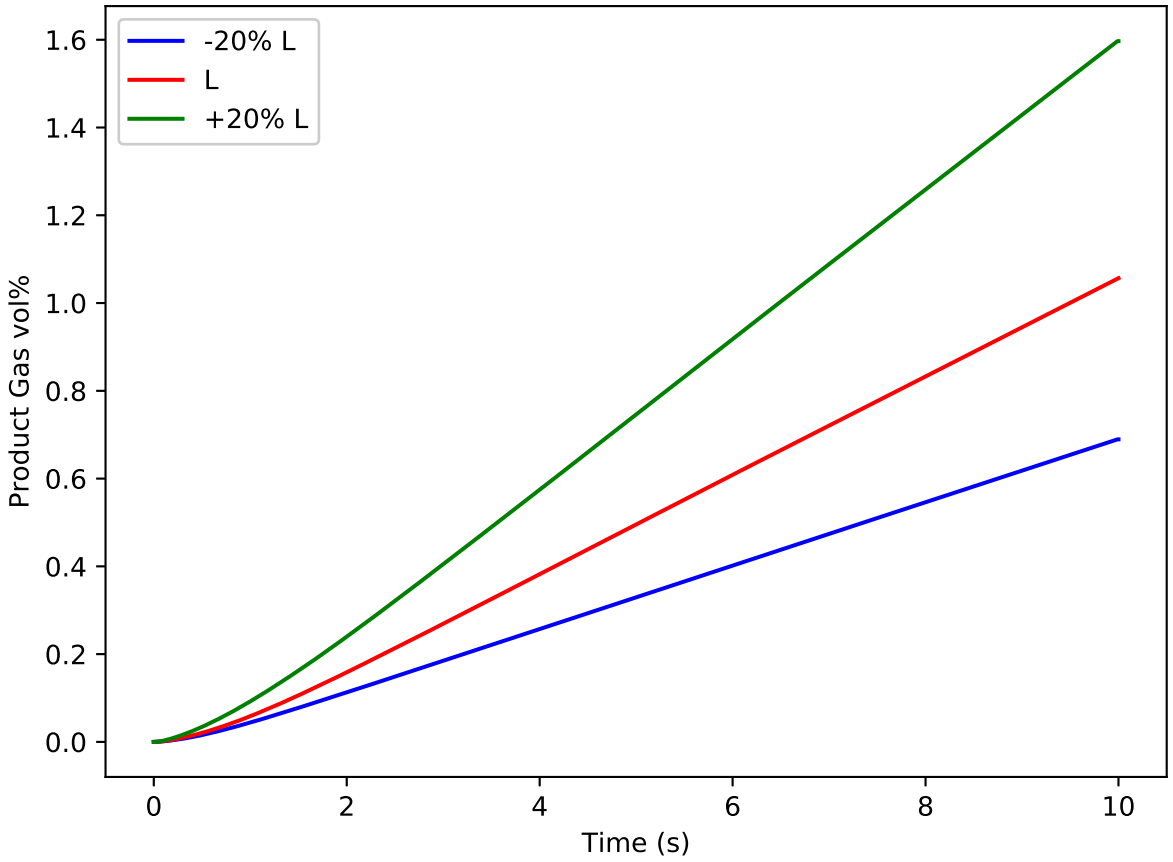

Figure 3.9: Sensitivity analysis: length of the pore

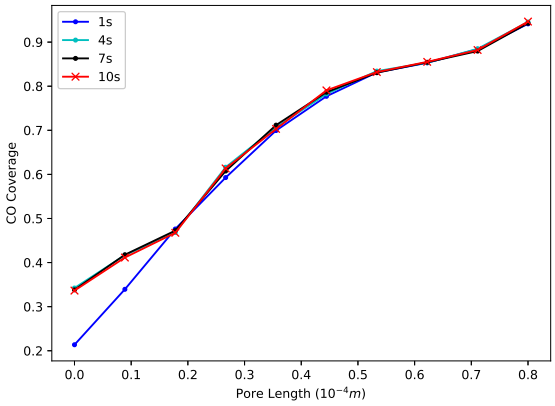

(a) CO coverage (-20% L)

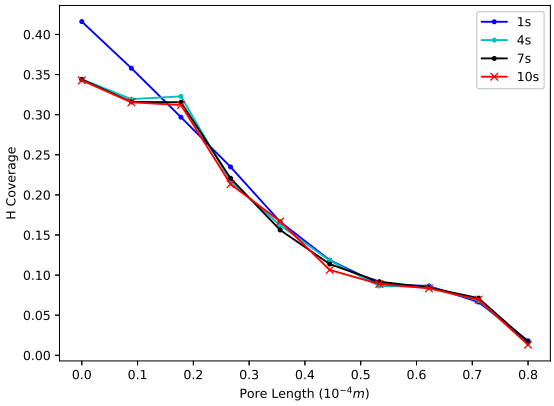

(b) H coverage (-20% L)

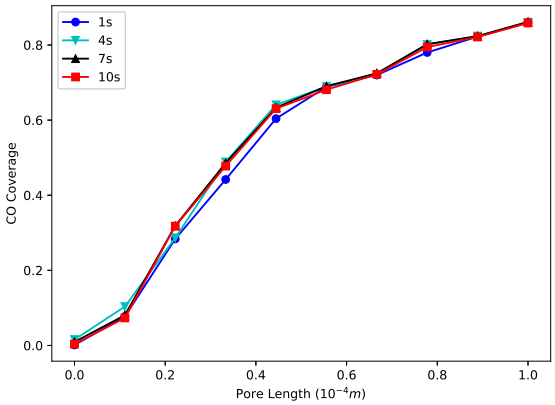

(c) CO coverage (L)

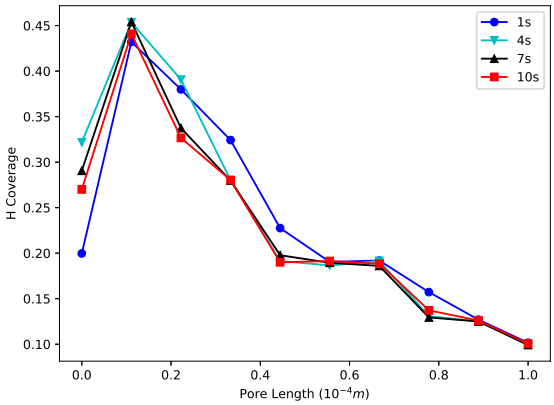

(d) H coverage (L)

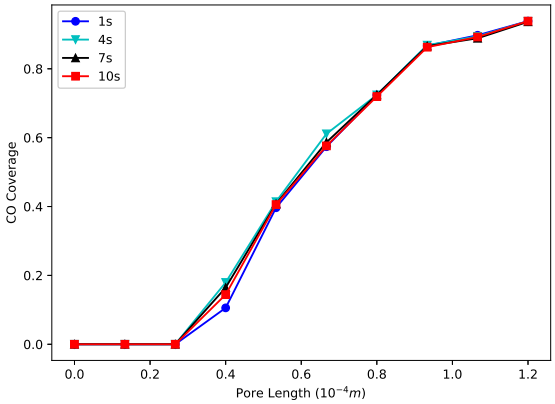

(e) CO coverage (+20% L)

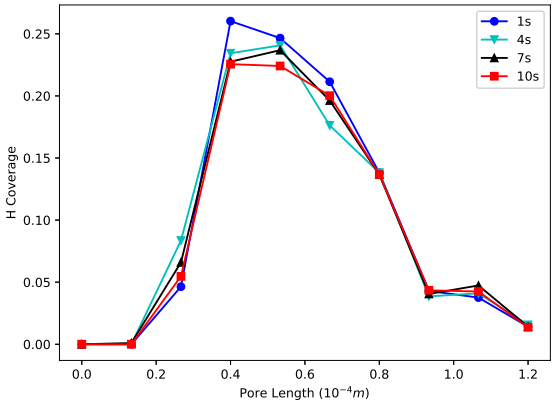

(f) H coverage (+20% L)

Figure 3.10: Surface coverage profile with varying pore lengths

simulation and consequently the increment in CO and H atoms on the surface accelerates the surface reaction process.

The surface coverage profiles of CO and H are also presented in Figure 3.12. The effect of porosity is significant near to the particle center. Compared to the reference surface coverage profile, the fuel gas cannot reach the center of the particle by the end of the simulation when the porosity is reduced by 20%, whereas the overall surface coverage at the end of the pore is increased by over 50% when using + 20% porosity.

In this Chapter, a multiscale particle modelling framework consisting of a gas diffusion model and a surface reaction model has been developed for oxygen carrier particles used in a typical CLC system. Chemical reaction kinetics are explicitly considered in the surface model using reaction rate constants obtained from DFT analysis. These reaction rate constants are then modified for the purpose of sensitivity analysis. Simulation results obtained from kMC-based model showed better qualitative agreement with the experimental data reported in the literature. Due to the lack of similar OC particle models or directly comparable experimental data for the simulated NiO system, detailed model validation cannot be performed at the moment. However, the sensitivity analysis of the influence of pore length and particle porosity has showed reasonable tendencies and responses, which indicates the feasibility of this model.

Parameters ($m^2 \cdot s^{-1}$)	Values
$\mathcal{D}_{e,CO}$	5.18×10^{-7}
$\mathcal{D}_{e,CO_2}$	4.13×10^{-7}
$\mathcal{D}_{e,H_2}$	1.94×10^{-6}
$\mathcal{D}_{e,H_2O}$	6.46×10^{-7}

Table 3.5: Effective Diffusivity (-20% ρ)

Parameters ($m^2 \cdot s^{-1}$)	Values
$\mathcal{D}_{e,CO}$	1.17×10^{-6}
$\mathcal{D}_{e,CO_2}$	9.30×10^{-7}
$\mathcal{D}_{e,H_2}$	4.36×10^{-6}
$\mathcal{D}_{e,H_2O}$	1.45×10^{-6}

Table 3.6: Effective Diffusivity (+20% ρ)

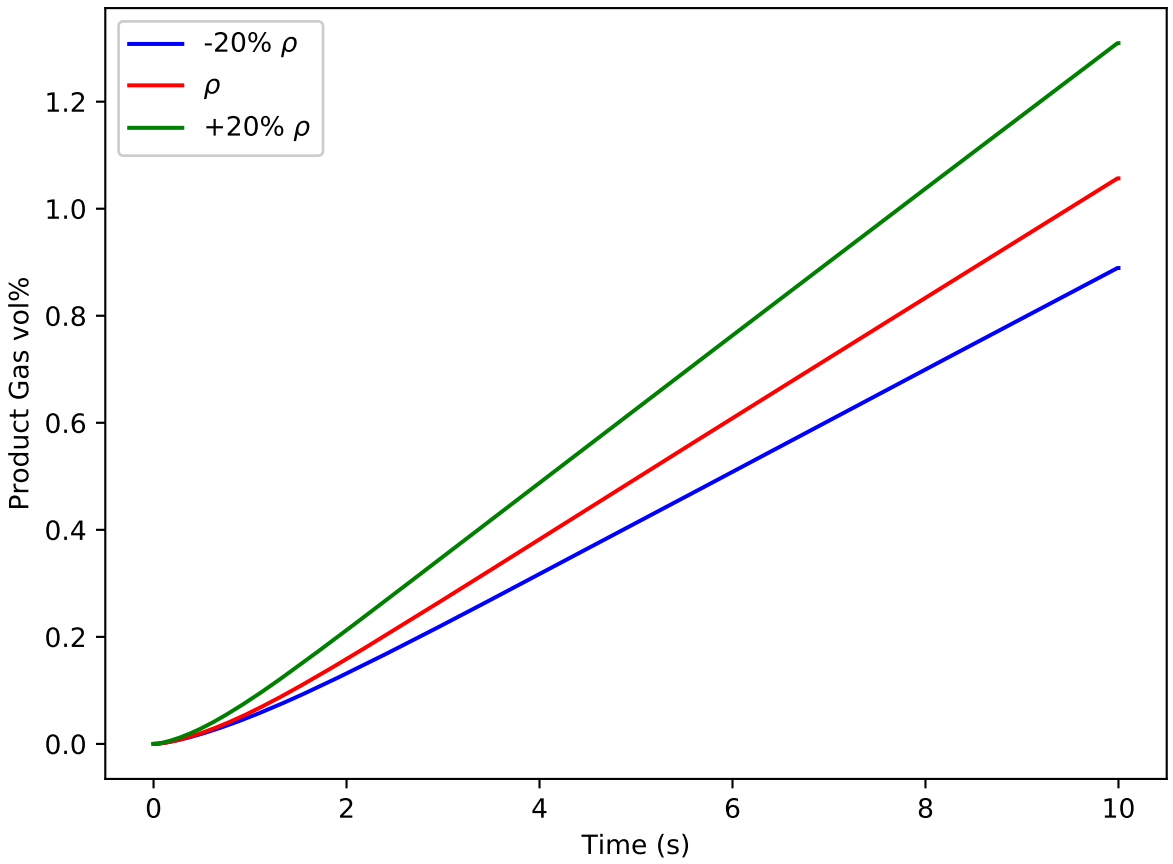

Figure 3.11: Sensitivity analysis: porosity of the particle

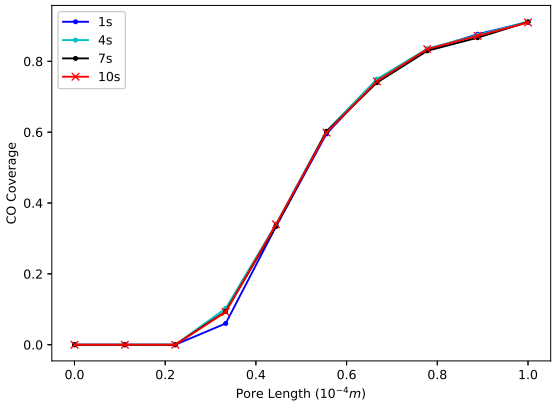

(a) CO coverage (-20% ρ)

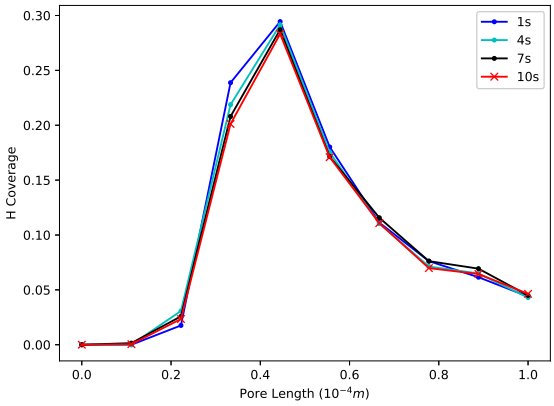

(b) H coverage (-20% ρ)

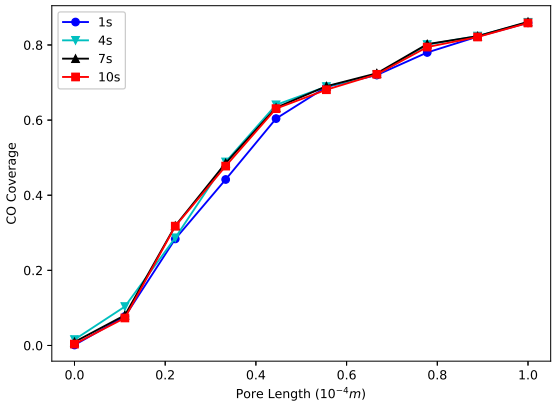

(c) CO coverage (ρ)

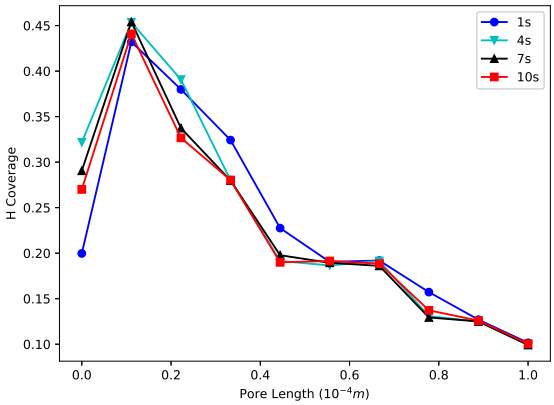

(d) H coverage (ρ)

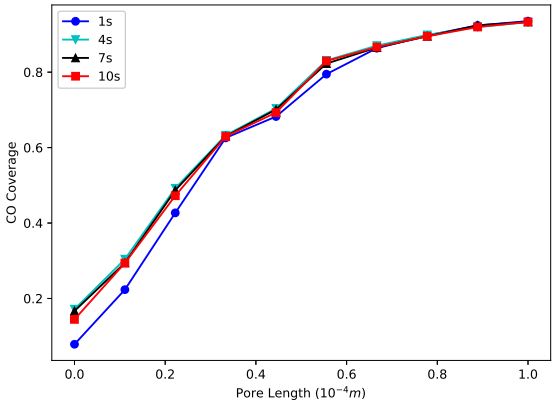

(e) CO coverage (+20% ρ)

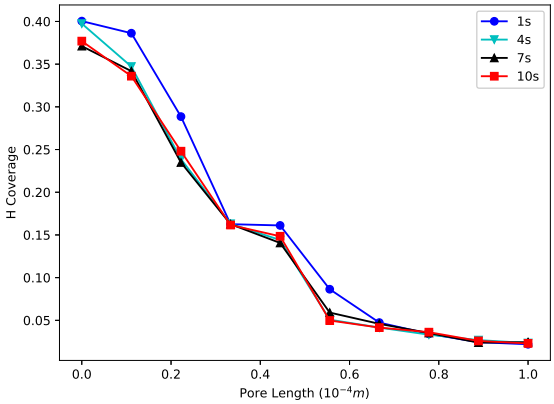

(f) H coverage (+20% ρ)

Figure 3.12: Surface coverage profile with varying particle porosities

Chapter 4

Conclusions and Future work

This thesis presented a multiscale modelling framework for oxygen carrier particles used in the CLC process. Compared to other existing OC models, the main advantage of this model is that it is able to explicitly consider the effect of elementary reactions involved in the overall reaction. The multiscale model consists of mass balance equations that describe intra-particle gas diffusion (*i.e.*, macroscale) and statistical techniques MFA and kMC to estimate the averaged nanoscopic behaviour of all the elementary reactions taking place on interstitial surface of the OC particle (*i.e.*, microscale). Chemical reaction kinetics described by microscale model are obtained from DFT analysis.

In the present work, NiO was selected to be the solid reactant that provides oxygen, and syngas was chosen to be the gas reactant (fuel gas). Simulation results and experimental data were compared and sensitivity analysis was conducted to test the quality of the multiscale model presented in this work. The main conclusions are summarized as follows:

- Compared to experimental data that uses similar OC particle material and fuel gas, simulation results obtained from kMC-based multiscale model qualitatively agrees with the experimental data. On the other hand, MFA-based model is less sensitive to the changes in fuel gas composition due to the absence of lateral interactions. In other words, kMC-based model is able to provide better results by considering reaction details that are difficult to describe by the MFA-based model.

- While performing a sensitivity analysis, the model showed reasonable tendencies and responses to the changes in chemical reaction rate constants, pore length, as well as particle porosity. More specifically, increasing reaction rate constants, pore length, and particle porosity increases the generation rate of CO_2 and H_2O by enhancing

the speed of surface reactions, available solid reactant content and intra-particle gas transportation process, respectively. These results indicate that the implementation of the multiscale modelling scheme proposed in this study is successful. To the author's knowledge, this is the first multiscale model for an OC particle in the CLC process.

- Significant changes in product generation rate were observed after the modification of chemical reaction constants, which suggests that surface reaction mechanism plays an important role in the overall CLC process. This model can be used to provide insights of elementary surface reactions and therefore enable the design of ideal OC particle at atomic scale.

4.1 Future work

Despite its novelty and potential, the proposed model can still be improved in many ways; hence, many modifications, tests, and adaptations have been left for future work:

1. First of all, one of the main issues that makes model validation difficult is the assumption of excess oxygen on the surface. In order to keep this assumption valid during the simulation, the model can only be used to simulate the early stages of the reaction and the complete solid conversion can never be achieved. To remove this assumption, knowledge of the mechanism and kinetics of the lattice diffusion of oxygen atom is required. The kMC algorithm should also be modified correspondingly to include the oxygen transport and also allow vacancy defects to exist on the lattice surface.

2. The effect of nearest neighbors is currently considered using educated guesses. In reality, those effects can be drastically different than those assumed here. For example, having one nearest neighbor may simply raise or lower the energy barrier for the reaction path, but can also change the shape of the potential energy surface. Moreover, the effect of nearest neighbors is likely not as exponential as it is assumed in the model. To improve the accuracy of kMC simulation, the DFT analysis presented in Section 3.1.2 must be extended to consider such events.

3. The elementary reactions described by kMC simulations are derived from results of first-principles calculations. Some assumptions were made in these calculations that may have affected the accuracy of the results. The possible causes of the inaccuracy

are explained in Section 2.5 and are beyond the scope of this thesis. However, additional reaction details can be considered in kMC simulation once the DFT analysis become available.

4. The modelling framework can be applied to other gas-solid systems. One of the advantages of this modelling scheme is that the chemical kinetics are obtained from first-principles calculations. In other words, model fitting with experimental data is not necessary for the model development as long as the reaction kinetics can be provided by DFT analysis. This characteristic reduces the time and cost associated with conducting experiments using numerous materials under different operating conditions. However, that does not mean the experiment is not important. In fact, the model and the experiment are both essential to the development of OC particles. The experiment provides real-life data that indicates the quality of the model, while the model predicts the effect of certain parameters and guides the experiments.

Regarding the application of the proposed model, because of its reasonable computational time, it can be integrated into the mass balance equation of a reactor model and predict the consumption and generation rate of the fuel and product gas, respectively. On the other hand, the model can provide an estimate of the overall effect of all the elementary reactions over a period of time that is orders of magnitude longer than the characteristic time scale of each elementary reaction. Therefore, when the experimental data are available, a comparison between simulation results and experimental data can be used as an indicator of the validity of the reaction mechanism established by DFT analysis. Alternatively, the model is also a suitable tool for top-down optimization in which a predetermined target (*e.g.* increasing selectivity or reactivity) is achieved by searching for materials with desired electronic properties based on first-principles calculations.

References

[1] Anders Lyngfelt, Bo Leckner, and Tobias Mattisson. A fluidized-bed combustion process with inherent CO_2 separation; application of chemical-looping combustion. *Chemical Engineering Science*, 56(10):3101 – 3113, 2001.

[2] Yoshio NAKANO, Shinji IWAMOTO, Takashi MAEDA, Masaru ISHIDA, and Takashi AKEHATA. Characteristics of reduction and oxidization cyclic process by use of αfe2o3 medium. *Tetsu-to-Hagane*, 72(10):1521–1528, 1986.

[3] Tobias Mattisson, Anders Lyngfelt, and Paul Cho. The use of iron oxide as an oxygen carrier in chemical-looping combustion of methane with inherent separation of co2. *Fuel*, 80(13):1953 – 1962, 2001.

[4] Luis F De Diego, Francisco Garcıa-Labiano, Juan Adánez, Pilar Gayán, Alberto Abad, Beatriz M Corbella, and Jose Marıa Palacios. Development of cu-based oxygen carriers for chemical-looping combustion. *Fuel*, 83(13):1749–1757, 2004.

[5] Tobias Mattisson, Marcus Johansson, and Anders Lyngfelt. The use of nio as an oxygen carrier in chemical-looping combustion. *Fuel*, 85(5-6):736–747, 2006.

[6] Paul Cho, Tobias Mattisson, and Anders Lyngfelt. Comparison of iron-, nickel-, copper-and manganese-based oxygen carriers for chemical-looping combustion. *Fuel*, 83(9):1215–1225, 2004.

[7] He Fang, Li Haibin, and Zhao Zengli. Advancements in development of chemical-looping combustion: a review. *International Journal of Chemical Engineering*, 2009, 2009.

[8] Ho-Jung Ryu, Dal-Hee Bae, Keun-Hee Han, Seung-Yong Lee, Gyoung-Tae Jin, and Jeong-Hoo Choi. Oxidation and reduction characteristics of oxygen carrier particles and reaction kinetics by unreacted core model. *Korean Journal of Chemical Engineering*, 18(6):831–837, nov 2001.

[9] Francisco García-Labiano, Luis F. de Diego, Juan Adánez, Alberto Abad, and Pilar Gayán. Temperature variations in the oxygen carrier particles during their reduction and oxidation in a chemical-looping combustion system. *Chemical Engineering Science*, 60(3):851–862, 2005.

[10] Mohammad M. Hossain and Hugo I. de Lasa. Reduction and oxidation kinetics of Co-Ni/Al_2O_3 oxygen carrier involved in a chemical-looping combustion cycles. *Chemical Engineering Science*, 65(1):98–106, jan 2010.

[11] Ho-Jung Ryu, Dal-Hee Bae, and Gyoung-Tae Jin. Effect of temperature on reduction reactivity of oxygen carrier particles in a fixed bed chemical-looping combustor. *Korean Journal of Chemical Engineering*, 20(5):960–966, 2003.

[12] MM Hossain, KE Sedor, and HI De Lasa. Co–ni/al2o3 oxygen carrier for fluidized bed chemical-looping combustion: desorption kinetics and metal–support interaction. *Chemical Engineering Science*, 62(18-20):5464–5472, 2007.

[13] Pilar Gayán, F Luis, Francisco García-Labiano, Juan Adánez, Alberto Abad, and Cristina Dueso. Effect of support on reactivity and selectivity of ni-based oxygen carriers for chemical-looping combustion. *Fuel*, 87(12):2641–2650, 2008.

[14] Cristina Dueso, María Ortiz, Alberto Abad, Francisco García-Labiano, Luis F. de Diego, Pilar Gayán, and Juan Adánez. Reduction and oxidation kinetics of nickel-based oxygen-carriers for chemical-looping combustion and chemical-looping reforming. *Chemical Engineering Journal*, 188:142–154, apr 2012.

[15] J. Blunden, D. S. Arndt, and Eds. State of the climate in 2017. *Bulletin of the American Meteorological Society*, 99(8), August 2018.

[16] Malte Meinshausen, Nicolai Meinshausen, William Hare, Sarah C. B. Raper, Katja Frieler, Reto Knutti, David J. Frame, and Myles R. Allen. Greenhouse-gas emission targets for limiting global warming to 2c. *Nature*, 458:1158, April 2009.

[17] Myles R. Allen, David J. Frame, Chris Huntingford, Chris D. Jones, Jason A. Lowe, Malte Meinshausen, and Nicolai Meinshausen. Warming caused by cumulative carbon emissions towards the trillionth tonne. *Nature*, 458:1163, April 2009.

[18] Juan Adánez, Alberto Abad, Francisco García-Labiano, Pilar Gayán, and Luis F. de Diego. Progress in chemical-looping combustion and reforming technologies. *Progress in Energy and Combustion Science*, 38(2):215–282, apr 2012.

[19] M. Ishida, D. Zheng, and T. Akehata. Evaluation of a chemical-looping-combustion power-generation system by graphic exergy analysis. *Energy*, 12(2):147 – 154, 1987.

[20] David C Thomas and Sally M Benson. *Carbon Dioxide Capture for Storage in Deep Geologic Formations-Results from the CO2 Capture Project: Vol 1-Capture and Separation of Carbon Dioxide from Combustion, Vol 2-Geologic Storage of Carbon Dioxide with Monitoring and Verification*. Elsevier, 2005.

[21] Liang-Shih Fan. *Chemical Looping Systems for Fossil Energy Conversions*. John Wiley & Sons, Inc., Hoboken, NJ, USA, sep 2010.

[22] A. Cuadrat, A. Abad, J. Adnez, L.F. de Diego, F. Garca-Labiano, and P. Gayn. Behavior of ilmenite as oxygen carrier in chemical-looping combustion. *Fuel Processing Technology*, 94(1):101 – 112, 2012.

[23] Henrik Leion, Anders Lyngfelt, Marcus Johansson, Erik Jerndal, and Tobias Mattisson. The use of ilmenite as an oxygen carrier in chemical-looping combustion. *Chemical Engineering Research and Design*, 86(9):1017 – 1026, 2008.

[24] Carl Linderholm, Matthias Schmitz, Pavleta Knutsson, and Anders Lyngfelt. Chemical-looping combustion in a 100-kw unit using a mixture of ilmenite and manganese ore as oxygen carrier. *Fuel*, 166:533 – 542, 2016.

[25] Henrik Leion, Tobias Mattisson, and Anders Lyngfelt. Use of ores and industrial products as oxygen carriers in chemical-looping combustion. *Energy & Fuels*, 23(4):2307–2315, 2009.

[26] Paul Cho, Tobias Mattisson, and Anders Lyngfelt. Comparison of iron-, nickel-, copper- and manganese-based oxygen carriers for chemical-looping combustion. *Fuel*, 83(9):1215 – 1225, 2004.

[27] J. Adánez, L. F. De Diego, F. García-Labiano, P. Gayán, A. Abad, and J. M. Palacios. Selection of oxygen carriers for chemical-looping combustion. *Energy & Fuels*, 18(2):371–377, Jan 2004.

[28] Tobias Mattisson, Marcus Johansson, and Anders Lyngfelt. The use of nio as an oxygen carrier in chemical-looping combustion. *Fuel*, 85(5):736 – 747, 2006.

[29] Tobias Mattisson, Anders Jrdns, and Anders Lyngfelt. Reactivity of some metal oxides supported on alumina with alternating methane and oxygenapplication for chemical-looping combustion. *Energy & Fuels*, 17(3):643–651, 2003.

[30] Laihong Shen, Jiahua Wu, Zhengping Gao, and Jun Xiao. Reactivity deterioration of nio/al2o3 oxygen carrier for chemical looping combustion of coal in a 10kwth reactor. *Combustion and Flame*, 156(7):1377 – 1385, 2009.

[31] Masaru Ishida, Hongguang Jin, and Toshihiro Okamoto. A fundamental study of a new kind of medium material for chemical-looping combustion. *Energy & Fuels*, 10(4):958–963, 1996.

[32] Masaru Ishida, Hongguang Jin, and Toshihiro Okamoto. Kinetic behavior of solid particle in chemical-looping combustion: suppressing carbon deposition in reduction. *Energy & Fuels*, 12(2):223–229, 1998.

[33] Raffaella Villa, Cinzia Cristiani, Gianpiero Groppi, Luca Lietti, Pio Forzatti, Ugo Cornaro, and Stefano Rossini. Ni based mixed oxide materials for ch4 oxidation under redox cycle conditions. *Journal of Molecular Catalysis A: Chemical*, 204-205:637 – 646, 2003. In honour of Prof. R. Ugo on the occasion of his 65th. Birthday.

[34] Pilar Gayn, Cristina Dueso, Alberto Abad, Juan Adanez, Luis F. de Diego, and Francisco Garca-Labiano. Nio/al2o3 oxygen carriers for chemical-looping combustion prepared by impregnation and depositionprecipitation methods. *Fuel*, 88(6):1016 – 1023, 2009.

[35] Kelly E. Sedor, Mohammad M. Hossain, and Hugo I. de Lasa. Reactivity and stability of ni/al2o3 oxygen carrier for chemical-looping combustion (clc). *Chemical Engineering Science*, 63(11):2994 – 3007, 2008.

[36] Cristina Dueso, Alberto Abad, Francisco Garca-Labiano, Luis F. de Diego, Pilar Gayn, Juan Adnez, and Anders Lyngfelt. Reactivity of a nio/al2o3 oxygen carrier prepared by impregnation for chemical-looping combustion. *Fuel*, 89(11):3399 – 3409, 2010.

[37] Shunji Homma, Shinji Ogata, Jiro Koga, and Shiro Matsumoto. Gas–solid reaction model for a shrinking spherical particle with unreacted shrinking core. *Chemical Engineering Science*, 60(18):4971–4980, 2005.

[38] Christos Georgakis, C.W. Chang, and J. Szekely. A changing grain size model for gassolid reactions. *Chemical Engineering Science*, 34(8):1072 – 1075, 1979.

[39] W. Kohn and L. J. Sham. Self-consistent equations including exchange and correlation effects. *Phys. Rev.*, 140:A1133–A1138, Nov 1965.

[40] P. Hohenberg and W. Kohn. Inhomogeneous electron gas. *Phys. Rev.*, 136:B864–B871, Nov 1964.

[41] Karsten Reuter, Daan Frenkel, and Matthias Scheffler. The steady state of heterogeneous catalysis, studied by first-principles statistical mechanics. *Phys. Rev. Lett.*, 93:116105, Sep 2004.

[42] Andreas Eichler. Co oxidation on transition metal surfaces: reaction rates from first principles. *Surface Science*, 498(3):314 – 320, 2002.

[43] Ya-Ling Song, Li-Li Yin, Jie Zhang, P. Hu, Xue-Qing Gong, and Guanzhong Lu. A dft+u study of co oxidation at ceo2(110) and (111) surfaces with oxygen vacancies. *Surface Science*, 618:140 – 147, 2013.

[44] K. Honkala, A. Hellman, I. N. Remediakis, A. Logadottir, A. Carlsson, S. Dahl, C. H. Christensen, and J. K. Nørskov. Ammonia synthesis from first-principles calculations. *Science*, 307(5709):555–558, 2005.

[45] Ping Liu and Jos A. Rodriguez. Water-gas-shift reaction on metal nanoparticles and surfaces. *The Journal of Chemical Physics*, 126(16):164705, 2007.

[46] Jingde Li, Eric Croiset, and Luis Ricardez-Sandoval. Theoretical investigation of the methane cracking reaction pathways on ni (111) surface. *Chemical Physics Letters*, 639:205 – 210, 2015.

[47] Daan Frenkel and Berend Smit. *Understanding Molecular Simulation*. Academic Press, Inc., Orlando, FL, USA, 2nd edition, 2001.

[48] I. Kevrekidis, L.D. Schmidt, and R. Aris. Rate multiplicity and oscillations in single species surface reactions. *Surface Science*, 137(1):151 – 166, 1984.

[49] Arthur F. Voter. Introduction to the kinetic monte carlo method. In Kurt E. Sickafus, Eugene A. Kotomin, and Blas P. Uberuaga, editors, *Radiation Effects in Solids*, pages 1–23, Dordrecht, 2007. Springer Netherlands.

[50] Michael P Allen et al. Introduction to molecular dynamics simulation. *Computational soft matter: from synthetic polymers to proteins*, 23:1–28, 2004.

[51] M. Born and R. Oppenheimer. Zur quantentheorie der molekeln. *Annalen der Physik*, 389(20):457–484, 1927.

[52] Alan D McNaught and Alan D McNaught. *Compendium of chemical terminology*, volume 1669. Blackwell Science Oxford, 1997.

[53] Henry Eyring. The activated complex in chemical reactions. *The Journal of Chemical Physics*, 3(2):107–115, 1935.

[54] Keith J. Laidler and M. Christine King. Development of transition-state theory. *The Journal of Physical Chemistry*, 87(15):2657–2664, 1983.

[55] S. R. Blaszkowski, A. P. J. Jansen, M. A. C. Nascimento, and R. A. van Santen. Density functional theory calculations of the transition states for hydrogen exchange and dehydrogenation of methane by a broensted zeolitic proton. *The Journal of Physical Chemistry*, 98(49):12938–12944, 1994.

[56] Nicolaas Godfried Van Kampen. *Stochastic processes in physics and chemistry*, volume 1. Elsevier, 1992.

[57] D. Freedman. *Markov Chains*. Holden-Day series in probability and statistics. Springer New York, 2012.

[58] Antonius Petrus Johannes Jansen. *An introduction to kinetic Monte Carlo simulations of surface reactions*, volume 856. Springer, 2012.

[59] D. G. Vlachos. Multiscale integration hybrid algorithms for homogeneous–heterogeneous reactors. *AIChE Journal*, 43(11):3031–3041, nov 1997.

[60] C Schaefer and APJ Jansen. Coupling of kinetic monte carlo simulations of surface reactions to transport in a fluid for heterogeneous catalytic reactor modeling. *The Journal of chemical physics*, 138(5):054102, 2013.

[61] Panagiotis D Christofides. Control of nonlinear distributed process systems: Recent developments and challenges. *AIChE Journal*, 47(3):514–518, 2001.

[62] Timothy O Drews, Eric G Webb, David L Ma, Jay Alameda, Richard D Braatz, and Richard C Alkire. Coupled mesoscalecontinuum simulations of copper electrodeposition in a trench. *AIChE journal*, 50(1):226–240, 2004.

[63] Yiming Lou and Panagiotis D Christofides. Feedback control of growth rate and surface roughness in thin film growth. *AIChE Journal*, 49(8):2099–2113, 2003.

[64] DG Vlachos. Multiscale integration hybrid algorithms for homogeneous–heterogeneous reactors. *AIChE Journal*, 43(11):3031–3041, 1997.

[65] Ioannis G Kevrekidis, C William Gear, and Gerhard Hummer. Equation-free: The computer-aided analysis of complex multiscale systems. *AIChE Journal*, 50(7):1346–1355, 2004.

[66] E Weinan, Bjorn Engquist, and Zhongyi Huang. Heterogeneous multiscale method: a general methodology for multiscale modeling. *Physical Review B*, 67(9):092101, 2003.

[67] Jingde Li, Eric Croiset, and Luis Ricardez-Sandoval. Carbon nanotube growth: First-principles-based kinetic monte carlo model. *Journal of Catalysis*, 326:15–25, 2015.

[68] Shabnam Rasoulian and Luis Alberto Ricardez-Sandoval. Uncertainty analysis and robust optimization of multiscale process systems with application to epitaxial thin film growth. *Chemical Engineering Science*, 116:590–600, 2014.

[69] Shabnam Rasoulian and Luis A Ricardez-Sandoval. A robust nonlinear model predictive controller for a multiscale thin film deposition process. *Chemical Engineering Science*, 136:38–49, 2015.

[70] Shabnam Rasoulian and Luis A Ricardez-Sandoval. Stochastic nonlinear model predictive control applied to a thin film deposition process under uncertainty. *Chemical Engineering Science*, 140:90–103, 2016.

[71] Donovan Chaffart and Luis A Ricardez-Sandoval. Optimization and control of a thin film growth process: A hybrid first principles/artificial neural network based multiscale modelling approach. *Computers & Chemical Engineering*, 119:465–479, 2018.

[72] Grigoriy Kimaev and Luis A Ricardez-Sandoval. A comparison of efficient uncertainty quantification techniques for stochastic multiscale systems. *AIChE Journal*, 63(8):3361–3373, 2017.

[73] Grigoriy Kimaev and Luis A Ricardez-Sandoval. Multilevel monte carlo for noise estimation in stochastic multiscale systems. *Chemical Engineering Research and Design*, 140:33–43, 2018.

[74] QH Zeng, AB Yu, and GQ Lu. Multiscale modeling and simulation of polymer nanocomposites. *Progress in polymer science*, 33(2):191–269, 2008.

[75] Donovan Chaffart, Shabnam Rasoulian, and Luis A Ricardez-Sandoval. Distributional uncertainty analysis and robust optimization in spatially heterogeneous multiscale process systems. *AIChE Journal*, 62(7):2374–2390, 2016.

[76] Donovan Chaffart and Luis A Ricardez-Sandoval. Robust dynamic optimization in heterogeneous multiscale catalytic flow reactors using polynomial chaos expansion. *Journal of Process Control*, 60:128–140, 2017.

[77] Martin Anton van der Hoef, M van Sint Annaland, NG Deen, and JAM Kuipers. Numerical simulation of dense gas-solid fluidized beds: a multiscale modeling strategy. *Annu. Rev. Fluid Mech.*, 40:47–70, 2008.

[78] Dionisios G Vlachos. A review of multiscale analysis: examples from systems biology, materials engineering, and other fluid–surface interacting systems. *Advances in Chemical Engineering*, 30:1–61, 2005.

[79] Abhijit Chatterjee and Dionisios G Vlachos. An overview of spatial microscopic and accelerated kinetic monte carlo methods. *Journal of computer-aided materials design*, 14(2):253–308, 2007.

[80] Luis A Ricardez-Sandoval. Current challenges in the design and control of multiscale systems. *The Canadian Journal of Chemical Engineering*, 89(6):1324–1341, 2011.

[81] D.G. Vlachos, A.B. Mhadeshwar, and N.S. Kaisare. Hierarchical multiscale model-based design of experiments, catalysts, and reactors for fuel processing. *Computers & Chemical Engineering*, 30(10):1712 – 1724, 2006. Papers form Chemical Process Control VII.

[82] Huabei You, Yue Yuan, Jingde Li, and Luis Ricardez Sandoval. A multi-scale model for co2 capture: A nickel-based oxygen carrier in chemical-looping combustion. *IFAC-PapersOnLine*, 51(18):97–102, 2018.

[83] Edward N. Fuller, Paul D. Schettler, and J. Calvin. Giddings. New Method for Prediction of Binary Gas-phase Diffusion Coefficients. *Industrial & Engineering Chemistry*, 58(5):18–27, may 1966.

[84] H.S. Fogler. *Elements of Chemical Reaction Engineering*. Prentice Hall International Series in the Physical and Chemi. Prentice Hall, 2016.

[85] P. E. Blöchl. Projector augmented-wave method. *Physical Review B*, 50(24):17953–17979, dec 1994.

[86] John P. Perdew, Kieron Burke, and Matthias Ernzerhof. Generalized Gradient Approximation Made Simple. *Physical Review Letters*, 77(18):3865–3868, oct 1996.

[87] Graeme Henkelman, Blas P. Uberuaga, and Hannes Jónsson. A climbing image nudged elastic band method for finding saddle points and minimum energy paths. *The Journal of Chemical Physics*, 113(22):9901–9904, 2000.

[88] C.William Gear, Ju Li, and Ioannis G Kevrekidis. The gap-tooth method in particle simulations. *Physics Letters A*, 316(3):190–195, Sep 2003.

[89] T. Okazawa, T. Nishizawa, T. Nishimura, and Y. Kido. Oxidation kinetics for Ni(111) and the structure of the oxide layers. *Phys. Rev. B*, 75:033413, Jan 2007.

[90] Alberto Abad, Francisco García-Labiano, Luis F de Diego, Pilar Gayán, and Juan Adánez. Reduction kinetics of cu-, ni-, and fe-based oxygen carriers using syngas (co+ h2) for chemical-looping combustion. *Energy & Fuels*, 21(4):1843–1853, 2007.

[91] Aron J Cohen, Paula Mori-Sánchez, and Weitao Yang. Insights into current limitations of density functional theory. *Science*, 321(5890):792–794, 2008.

[92] David M Golden. Experimental and theoretical examples of the value and limitations of transition state theory. *Journal of Physical Chemistry*, 83(1):108–113, 1979.

[93] Donald G Truhlar, Bruce C Garrett, and Stephen J Klippenstein. Current status of transition-state theory. *The Journal of physical chemistry*, 100(31):12771–12800, 1996.

[94] Yue Yuan, Huabei You, and Luis Ricardez-Sandoval. Recent advances on first-principles modeling for the design of materials in co2 capture technologies. *Chinese Journal of Chemical Engineering*, 2018.

[95] B. Jankovi, B. Adnaevi, and S. Mentus. The kinetic study of temperature-programmed reduction of nickel oxide in hydrogen atmosphere. *Chemical Engineering Science*, 63(3):567 – 575, 2008.

[96] Jos A. Rodriguez, Jonathan C. Hanson, Anatoly I. Frenkel, Jae Y. Kim, and Manuel Prez. Experimental and theoretical studies on the reaction of h2 with nio: role of o vacancies and mechanism for oxide reduction. *Journal of the American Chemical Society*, 124(2):346–354, 2002. PMID: 11782187.

[97] Cristina Dueso, Mara Ortiz, Alberto Abad, Francisco Garca-Labiano, Luis F. de Diego, Pilar Gayn, and Juan Adnez. Reduction and oxidation kinetics of nickel-based oxygen-carriers for chemical-looping combustion and chemical-looping reforming. *Chemical Engineering Journal*, 188:142 – 154, 2012.

[98] Daniel T Gillespie. A general method for numerically simulating the stochastic time evolution of coupled chemical reactions. *Journal of Computational Physics*, 22(4):403 – 434, 1976.

[99] K.J. Laidler and John H. Meiser. *Physical chemistry*. Benjamin/Cummings Pub. Co., 1982.

[100] S. Raimondeau, D. Norton, D.G. Vlachos, and R.I. Masel. Modeling of high-temperature microburners. *Proceedings of the Combustion Institute*, 29(1):901 – 907, 2002. Proceedings of the Combustion Institute.

[101] Mohammad M. Hossain and Hugo I. de Lasa. Chemical-looping combustion (CLC) for inherent CO_2 separations—a review. *Chemical Engineering Science*, 63(18):4433–4451, 2008.

[102] Tobias Mattisson, Marcus Johansson, and Anders Lyngfelt. The use of NiO as an oxygen carrier in chemical-looping combustion. *Fuel*, 85(5-6):736–747, mar 2006.

[103] Masaru Ishida and Hongguang Jin. A novel chemical-looping combustor without NO_x formation. *Industrial & Engineering Chemistry Research*, 35(7):2469–2472, July 1996.

[104] M Ishida and H Jin. CO_2 recovery in a power plant with chemical looping combustion. *Energy Conversion and Management*, 38:S187–S192, Jan 1997.